Published OnlineFirst February 4, 2019; DOI: 10.1158/0008-5472.CAN-18-0881

Tumor Biology and Immunology

Cancer Research

Targeting APLN/APLNR Improves Antiangiogenic Efficiency and Blunts Proinvasive Side Effects of VEGFA/VEGFR2 Blockade in Glioblastoma

Giorgia Mastrella[1], Mengzhuo Hou[1], Min Li[1], Veit M. Stoecklein[2], Nina Zdouc[1], Marie N.M. Volmar[1], Hrvoje Miletic[3,4], Sören Reinhard[5], Christel C. Herold-Mende[6], Susanne Kleber[7], Katharina Eisenhut[1], Gaetano Gargiulo[8], Michael Synowitz[9], Angelo L. Vescovi[10], Patrick N. Harter[11], Josef M. Penninger[12], Ernst Wagner[5], Michel Mittelbronn[11,13], Rolf Bjerkvig[3], Dolores Hambardzumyan[14], Ulrich Schüller[15], Jörg-Christian Tonn[2], Josefine Radke[16], Rainer Glass[1,17,18], and Roland E. Kälin[1,18]

Abstract

Antiangiogenic therapy of glioblastoma (GBM) with bevacizumab, a VEGFA-blocking antibody, may accelerate tumor cell invasion and induce alternative angiogenic pathways. Here we investigate the roles of the proangiogenic apelin receptor APLNR and its cognate ligand apelin in VEGFA/VEGFR2 antiangiogenic therapy against distinct subtypes of GBM. In proneural GBM, apelin levels were downregulated by VEGFA or VEGFR2 blockade. A central role for apelin/APLNR in controlling GBM vascularization was corroborated in a serial implantation model of the angiogenic switch that occurs in human GBM. Apelin and APLNR are broadly expressed in human GBM, and knockdown or knockout of *APLN* in orthotopic models of proneural or classical GBM subtypes significantly reduced GBM vascularization compared with controls. However, reduction in apelin expression led to accelerated GBM cell invasion. Analysis of stereotactic GBM biopsies from patients as well as from *in vitro* and *in vivo* experiments revealed increased dissemination of APLNR-positive tumor cells when apelin levels were reduced. Application of apelin-F13A, a mutant APLNR ligand, blocked tumor angiogenesis and GBM cell invasion. Furthermore, cotargeting VEGFR2 and APLNR synergistically improved survival of mice bearing proneural GBM. In summary, we show that apelin/APLNR signaling controls GBM angiogenesis and invasion and that both pathologic features are blunted by apelin-F13A. We suggest that apelin-F13A can improve the efficiency and reduce the side effects of established antiangiogenic treatments for distinct GBM subtypes.

Significance: Pharmacologic targeting of the APLNR acts synergistically with established antiangiogenic treatments in glioblastoma and blunts therapy resistance to current strategies for antiangiogenesis.

See related commentary by Amoozgar et al., p. 2104

Introduction

Glioblastoma (GBM) is the most common and most malignant primary brain tumor (1). Current standard treatment consists of maximal resection followed by radiotherapy with concomitant temozolomide chemotherapy, if safe (2, 3). A subgroup of GBM is generated by epigenetic dysregulation (CpG-island methylator phenotype in isocitrate dehydrogenase mutant gliomas; IDH^{MUT}), but the majority of GBM represents

[1]Neurosurgical Research, Department of Neurosurgery, University Hospital, LMU Munich, Munich, Germany. [2]Department of Neurosurgery, University Hospital, LMU Munich, Munich, Germany. [3]Department of Biomedicine, University of Bergen, Bergen, Norway. [4]Department of Pathology, Haukeland University Hospital, Bergen, Norway. [5]Department of Pharmacy, LMU Munich, Munich, Germany. [6]Division of Neurosurgical Research, Department of Neurosurgery, University of Heidelberg, Germany. [7]Department of Molecular Neurobiology, German Cancer Research Center (DKFZ), Heidelberg, Germany. [8]Max Delbrück Center for Molecular Medicine, Berlin, Germany. [9]Department of Neurosurgery, University Hospital Center Schleswig Holstein, Kiel, Germany. [10]IRCCS Casa Sollievo della Sofferenza, San Giovanni Rotondo, Italy. [11]Edinger-Institute (Neurological Institute), Goethe-University Medical School, Frankfurt am Main, Germany and German Cancer Consortium (DKTK), partner site Frankfurt/Mainz; German Cancer Research Center (DKFZ), Heidelberg, Germany. [12]Institute of Molecular Biotechnology, Austrian Academy of Sciences, Vienna, Austria. [13]Luxembourg Centre of Neuropathology (LCNP), Luxembourg and NORLUX Neuro-Oncology Laboratory, Luxembourg Institute of Health (LIH), and Luxembourg Centre for Systems Biomedicine (LCSB), University of Luxembourg, Esch-sur-Alzette, Luxembourg. [14]Department of Pediatrics and Aflac Cancer Center of Children's Health Care of Atlanta, Emory University School of Medicine, Atlanta, Georgia. [15]Institute of Neuropathology and Department of Pediatric Haematology and Oncology, University Medical Center, Hamburg-Eppendorf and Research Institute Children's Cancer Center, Hamburg, Germany. [16]Department of Neuropathology, Charité-Universitätsmedizin Berlin, corporate member of Freie Universität Berlin, Humboldt-Universität zu Berlin, and Berlin Institute of Health, Berlin, German; Berlin Institute of Health (BIH), Berlin, Germany; German Cancer Consortium (DKTK), Heidelberg, Germany, Partner Site Berlin, Berlin, Germany. [17]German Cancer Consortium (DKTK), partner site Munich and German Cancer Research Center (DKFZ), Heidelberg, Germany. [18]Walter Brendel Center of Experimental Medicine, Faculty of Medicine, LMU Munich, Munich, Germany.

Note: Supplementary data for this article are available at Cancer Research Online (http://cancerres.aacrjournals.org/).

G. Mastrella, M. Hou, and M. Li contributed equally to this article.

Corresponding Author: Roland E. Kälin, University Hospital, LMU Munich, Marchioninistr. 15, Munich 81377, Germany. Phone: 4989-4400-73148; Fax: 4989-4400-77789; E-mail: roland.kaelin@med.lmu.de

doi: 10.1158/0008-5472.CAN-18-0881

Published OnlineFirst February 4, 2019; DOI: 10.1158/0008-5472.CAN-18-0881

IDH wild-type (WT) GBM (4), which can originate from neoplastic neural precursor cells (NPC; refs. 5, 6) after ablation or somatic mutation of the tumor suppressor p53, deletion of neurofibromatosis-1 (*NF1*), or loss of *CDKN2A*. Such genetic aberrations can coincide with loss of the *PTEN*. The vast majority of primary GBM is driven by genetic mutation in key tumor suppressor genes concomitant with accelerated activity of different proto-oncogenic signaling pathways (e.g., *EGFR* or platelet-derived growth factor receptor-A, *PDGFRA*) or through a mutant (ligand independent) form of *EGFR* (EGFR-variant-3, EGFRvIII; ref. 5).

Hallmarks of GBM include poorly-differentiated neoplastic astrocytes, increased cell proliferation, tumor necrosis, microvascular proliferation, and formation of an aberrant vasculature (1). Thus, antiangiogenic treatments appear to be a promising strategy for GBM (7). However, clinical studies using bevacizumab (AVAglio, RTOG-0825), a humanized mAb that blocks VEGFA signaling, did not improve overall survival in patients with GBM (8, 9). GBM often develops resistance to bevacizumab owing to upregulation of alternative proangiogenic pathways and the induction of tumor cell invasion (10). Moreover, differences in angiogenic responses could originate from interindividual GBM heterogeneity, as evidenced by the genetic stratification of GBM (11). The Cancer Genome Atlas (TCGA) revealed three subtypes of GBM, namely proneural, classical, and mesenchymal, which show differences in prognosis and response to treatment (4, 12). The neural GBM subtype was recently considered as a potential artefact (13). A retrospective analysis of the AVAglio trial indicated that patients with (IDH^{WT}) proneural GBM can benefit from bevacizumab by increased overall survival (14).

We previously hypothesized that the G-protein coupled receptor (GPCR) APJ (APLNR) and its cognate peptide-ligand apelin play some roles in tumor development (15). Here, apelin was undetectable in the healthy brain and APLNR mRNA expression was very low in normal brain vessels and we observed a dramatic upregulation of both apelin and APLNR in GBM -associated microvascular proliferations, as well as in radially oriented neoplastic cells surrounding band-like foci ("pseudopalisading necroses"). In hypoxic regions, apelin was highly coexpressed with VEGFA (15–17). In this context, it was suggested that apelin levels indicate improved tumor hypoxia due to vascular normalization upon bevacizumab treatment (18).

In this study using *in vitro* and *in vivo* models, we confirm that apelin/APLNR signaling has a strong proangiogenic role in proneural GBM. We show for the first time that blocking VEGFA/VEGFR2 signaling in GBM reduces apelin levels and accelerates the invasion of APLNR-expressing GBM cells. Importantly, administration of apelin-F13A, a mutant form of the natural apelin-13 peptide with avidity for APLNR (19), reduced tumor angiogenesis and cell invasion in GBM models, and had synergistic effects with VEGFR2 blockade.

Materials and Methods

Cell culture

GBM stem-like cell (GSC) were derived from human glioblastoma biopsies [as previously reported for NCH644 and NCH588J (20); GBM10, GBM13 and GBM14 (21); and GBM5av to 10av (22)] and were maintained under stem cell cultivation conditions in DMEM-F12 (catalog no. 11320-074) supplemented with 1 × B27 (catalog no. 17504-044), 5% penicillin–streptomycin (catalog no. 151140-122; all Thermo Fisher Scientific), 10 ng/mL epidermal growth factor (EGF; catalog no. 236-EG; Biotechne), and 10 ng/mL fibroblast growth factor (FGF; catalog no. 100-18B PeproTech). For all cultures, gene copy number analysis was performed and the *TP53*, *EGFR*, *PDGFRA*, *PIK3CA*, *PIK3R1*, *PIK3CG*, *PTEN*, *NF1*, *RB1*, *IDH1*, and *ATRX* loci were sequenced. We confirmed that all cultures were tumorigenic upon orthotopic implantation in immunodeficient mice. All of the GSCs, except for GBM10 cells, corresponded to the GBM subtype of the parental tumor.

NPCs were isolated from the subventricular zone of 5-day-old Bl6/J or FVB mice with homozygous deletion of *TP53* or *CDKN2A*. Isolated cells were cultured in spheroid conditions with DMEM-F12 medium supplemented with 1 × B27, 1% penicillin-streptomycin, 10 ng/mL EGF (catalogno. 236-EG; Biotechne) and 10 ng/mL FGF (catalog no. 100-18B; PeproTech). U87MG (HTB14) cells were obtained from the ATCC and cultured under adherent conditions in DMEM containing 1× MEM nonessential amino acids (catalog no. 11140-035), 5% penicillin–streptomycin, and 10% FBS (catalog no. 102270-106; all Thermo Fisher Scientific). GL261 cells were obtained from the National Cancer Institute, NCI-Frederick (Frederick, MD; Tumor Cell Repository) and maintained under neurosphere cell culture conditions as described above. All cells were maintained at 37°C in a humidified atmosphere of 95% O_2 and 5% CO_2. GSCs were validated repeatedly (2015 and 2017) by short tandem repeat (STR) fingerprinting (Eurofins Medignomix Forensik) and were regularly tested for *Mycoplasma* contamination by PCR.

Cell transduction

Mouse transgenic glioma cells as a model of the proneural GBM subtype ($p53^{KO}$*PDGFB* GSCs) were generated by transduction of a single-cell suspension of $p53^{KO}$ NPCs for 1 hour with a multiplicity of infection (MOI) of 80 of VSV-G pseudotyped GFP-PDGFB retroviral particles (kindly provided by F.Calzolari/M. Götz, Department of Physiological Genomics, LMU Munich, Munich, Germany). Human *PDGFB* cDNA was derived from the RCAS-pBIG plasmid (kindly provided by E. Holland, Fred Hutchinson Cancer Research Center Seattle). Transduction efficiency was verified by GFP immunofluorescence and was >99%. To study the influence of p53 status in the generated $p53^{KO}$*PDGFB* mouse GSCs, cells were transfected with lipofectamine (catalog no. 18324020; Thermo Fisher Scientific) and 3 μg of empty vector containing ampicillin-neomycin resistance, hotspot *p53* mutant (R172H, R175H, R248W, R249S, R270H, R273H, V143A) or wild-type *p53* plasmid DNA. Transfected GSCs were first selected for 4 weeks with 3 mg/mL of G418 antibiotics and selection was maintained using 1 mg/mL of G418.

As a model of the classical GBM subtype, $cdkn2a^{KO}$ NPCs were transfected with EGFRvIII-blasticidin/GFP plasmids to obtain $cdkn2a^{KO}$EGFRvIII GSCs. To obtain EGFRvIII-EGFR–overexpressing cells, cells were then transfected with 3 μg of neomycin-EGFR plasmid, and the cells were selected for 2 weeks with 1 mg/mL of Geneticin (catalog no. 10131027; Thermo Fisher Scientific). For proneural-like $p53^{KO}$EGFR GSCs, $p53^{KO}$NPCs were transfected with 3 μg of neomycin-EGFR plasmid and selected for 2 weeks with 1 mg/mL of Geneticin.

For gene silencing in GBM14 and NCH644, we used three different lentiviral shRNAmir constructs for apelin (AKD; catalog no. RHS4430: V3LHS_401190) or nonsilencing control (NSC;

Published OnlineFirst February 4, 2019; DOI: 10.1158/0008-5472.CAN-18-0881

catalog no. RHS4346) to produce viral particles in HEK293T cells with the TransLenti Viral GIPZ Packaging System (catalog no. TPLP4614, all Dharmacon GE Life Sciences) according to the manufacturer's instructions. Virus particle-containing supernatant was harvested 2 days after transfection, filtered with a 0.22-μm filter to avoid cellular contamination, and stored at −80°C. Primary GSC spheroids were dissociated with Accutase (catalog no. A6964; Sigma Aldrich), while U87MG cells were detached with trypsin/EDTA (catalog no. L2153; Merck Millipore). Then, 8×10^4 cells were incubated with 500 μL of virus particles at an MOI of 0.6–0.7 for 6 hours in a 24-well plate. Next, 1 mL of medium was added and the cells were left overnight at 37°C. The next day, the cells were centrifuged and resuspended in fresh medium. After cell recovery, cells were selected using puromycin (catalog no. P8833; Sigma Aldrich) for up to 3 weeks. The concentration of antibiotics was determined beforehand using a lethal dose curve. The efficiency of transduction/selection was >99%, as confirmed by FACS and immunofluorescence.

Animals

All experiments were performed in compliance with the National Guidelines for Animal Protection, Germany, with approval of the local animal care committee of the Government of Oberbayern (Regierung von Oberbayern). All experiments were conducted in accordance with the UK Coordinating Committee on Cancer Research guidelines (23). APLN-Knockout ($APLN^{KO}$) mice were obtained from J.M. Penninger (Institute of Molecular Biotechnology, Austrian Academy of Sciences, Vienna, Austria; ref. 24) and crossed with $Rag2^{KO}$ mice (B6.129S6-$Rag2^{tm1Fwa}$; ref. 25) kindly provided by G. Willimsky (Charité – Universitätsmedizin Berlin, Berlin, Germany) and previously purchased from Taconic. All mice had a C57Bl/6J background and genotyping was performed as previously described (24, 25). $Foxn1^{nu/nu}$ mice were ordered from Envigo. All mice were kept in a 12-hour light/dark cycle with *ad libitum* access to food and water. Mice were sacrificed at defined presymptomatic time points or at a humane endpoint in survival studies.

Tumor implantation

Mice were anesthetized with 7 μL/g of body weight of a mixture of xylazine (Rompun 2%; Bayer) and ketamine (Ketavet; Zoetis) in 0.9% NaCl. They were immobilized on a stereotactic frame (David Kopf Instruments) in flat-skull position and kept warm. A midline incision was made on the skull with a scalpel. To prevent the cornea from drying out, the eyes of the mice were covered with a moisturizing cream (Bepanthen; Bayer). Then, 1×10^5 (human) or 1×10^4 (mouse) cells/μL in supplement-free medium were implanted by stereotactic injection 1 mm anterior and 1.5 mm right to the bregma using a 22G Hamilton syringe (Hamilton) after drilling a hole into the skull with a 23G needle. At a depth of 4 mm, the cells were slowly injected within 2 minutes. After a settling period of another minute, the needle was removed at 1-mm steps/minute. The incision was sutured and patched with Opsite spray dressing (Smith & Nephew). Analgesia was achieved by administering a dose of 4 mg/kg before surgery and 2×2 mg/kg doses of intraperitoneal carprofen (Rymadil, Zoetis) for 3 days after surgery.

Intracerebral drug application

One day before implantation, mini-osmotic pumps were filled with 30 μg of apelin-F13A (Bachem) or 0.8 mg of DC101 (Eli Lilly) for sustained delivery over 14 days (Model 1002; Alzet) or 60 μg of apelin-F13A for sustained delivery over 28 days (Model 2004, Alzet) in artificial cerebrospinal fluid (aCSF; as described by Alzet) or with aCSF alone following priming overnight in aCSF at 37°C. The mini-osmotic pumps were implanted under anesthesia as described previously (26). For $p53^{KO}$PDGFB GBM treatment, 14-day pumps were implanted one week postimplantation, for GBM14 GBM 28-day pumps were implanted 2 weeks postimplantation. The needle of the brain infusion kit 3 (Alzet) was inserted into the hole originally prepared for orthotopic tumor implantation. The mice were sacrificed at the end of the pump's life (14 or 28 days) or at humane endpoints in survival studies.

Quantitative PCR

RNA was extracted using TRIzol (catalog no. 15596-026; Thermo Fisher Scientific) according to the manufacturer's instructions. Total RNA (1 μg) was reverse-transcribed into cDNA using a QuantiTect Reverse Transcription Kit (catalog no. 205313; Qiagen) and the cDNA was analyzed by quantitative PCR using TaqMan Gene Expression Assays for apelin (Hs00936329_m1; Mm00443562_m1; Rn00581093_m1), APLNR (Hs00945496_s1; Mm00442191_s1; Rn00580252_s1), KDR (Hs009117_m1; Rn00564986_m1), VEGFA (Hs00900054_m1), EG5 (Hs00189698_m1), and GAPDH (Hs99999905_m1; Mm99999915_g1; Rn01775763_g1) with TaqMan Gene Expression Master Mix (catalog no. 4369016) in a StepOnePlus Instrument (all Thermo Fisher Scientific). Samples were amplified using the standard running method within StepOne Software v2.2.2 by increasing the cycle number to 45. In each run, the expression levels of the target gene were normalized to those of *GAPDH* as a housekeeping gene.

Copy number analysis

Copy number analysis of all primary GBM was performed using Affymetrix Cytoscan HD Microarray at IMGM Laboratories. The array data are deposited at http://www.ebi.ac.uk/arrayexpress/ (Acc. E-MTAB-7649).

Viability and proliferation assays

For viability and proliferation assays, 6,000 cells/well were plated in 96-well plates in DMEM-F12 medium on day 0. Cell viability was measured after 24, 48, 72, and 96 hours using a MTT assay (CellTiter 96 Non-Radioactive Cell Proliferation Assay, catalog no. G4000; Promega) to assess cell metabolic activity. Cells were incubated for 1 hour with the Stop Mix solution. Absorbance was measured on a Versa Max microplate reader with SoftMax Pro software (Molecular Devices) at a reference wavelength of 630 nm. The background absorbance of wells containing cell-free supernatant was subtracted from all measurements. Six replicate samples were used in each experiment. Three experiments were performed for each cell type.

Invasion assays

For this assay, we used U87MG cells that had been maintained in spheroid conditions in DMEM-F12 medium. Spheroids were picked under an Axiovert25 microscope (Carl Zeiss). Spheroids were plated onto 24-well plates in 50 μL containing 1 mg/mL Rat Tail Collagen I (catalog no. A10483-01; Thermo Fisher Scientific), 10× PBS, 1 N NaOH, and diluted in bi-distilled water according to the manufacturer's instructions. As a chemoattractant source, the U87MG spheroids were added to the collagen

Published OnlineFirst February 4, 2019; DOI: 10.1158/0008-5472.CAN-18-0881

mix. Apelin-F13A was added at to the collagen mix at a concentration of 1 μmol/L. The collagen matrix was left to gel for 50 minutes at 37°C and then covered with 600 μL DMEM-F12 medium. Cell invasion was monitored for 7 days by taking photographs every day under an Axiovert25 microscope with Axiocam MRm and Axiovision Rel. 4.8 software (Carl Zeiss). The images were analyzed with ImageJ distribution Fiji and the invasive area (mm^2) was calculated as: ΔA = (area covered on day n) − (sphere area on day 0).

Human GBM specimens

The study was approved by the local Institutional Review Board of the LMU Munich (number 599-16, 18-304) and the UCT Frankfurt, Frankfurt am Main (GS4/09 SNO-6-2018) and agrees with all standards regarding the use of informed consent according to the guidelines of the local Institutional Review Board and the etical standards of the Helsinki Declaration. Informed written consent was obtained from all individual participants included in the study. GBM samples obtained from the Neurosurgery Department of the University Hospital, LMU Munich (Munich, Germany) were classified according to whether they were taken from the center or border of the original tumor mass at the time of surgical resection. Necrotic tumor tissue, as evaluated by H&E staining, was excluded from the analysis. Paraffin-embedded GBM samples were obtained from the Center for Neuropathology and Prion Research (ZNP), LMU Munich (Munich, Germany). For stereotactic biopsy, the surgical depth (the distance in mm from the target point 0 defined by the neurosurgeon) and the histopathologic description was recorded for each section obtained per specimen. Displayed in Fig. 3B are successive biopsies of the same patient taken along the stereotactic trajectory (*z*-axis), that were described by a neuropathologist to show a cell-dense pleomorphic glial tumor expressing glial fibrillary acidic protein (GFAP) and microtubule-associated protein 2 (MAP2), $IDH1^{WT}$, 15% Ki67-positive tumor cell nuclei, and numerous vascular proliferates from coordinate z = 0 until 3 mm toward the tumor border. From 5 mm to 8 mm along the *z*-axis, the biopsies contained central nervous system tissue with a progressively decreasing number of infiltrating glial tumor cells. Sections of patients pre- and post-bevacizumab treatment were obtained from the Edinger Institute, Frankfurt am Main. Quantification of pseudopalisading areas was performed in ImageJ using the threshold function on H&E overview images of the tumor area.

In situ hybridization

The work bench and instruments were carefully cleaned with RNAse-Zap (catalog no. R2020; Sigma Aldrich). Solutions were prepared using RNAse-free water and sterilized. Sections on slides were deparaffinized by serial passages into Roti-Histol and graded alcohol (100%–25%). Tissue was permeabilized by incubation for 10 minutes in 10 μg/mL proteinase K (catalog no. 04-1070; PeqLab, VWR). Slides were fixed for 10 minutes in 4% paraformaldehyde (PFA) and blocked for 10 minutes with acetic anhydride (0.25%; catalog no. 320102; Sigma Aldrich) in triethanolamine (1.5%; catalog no. 09278; Sigma Aldrich). Sections were dried for 2 hours at room temperature, incubated overnight at 65°C in a humidified chamber with digoxigenin (DIG)-labelled (DIG RNA labeling, cat. 11277073910; Roche Diagnostics) antisense or sense probes at a final concentration of 7 μg/mL, and diluted in a hybridization solution containing 100 μg/mL salmon sperm DNA (catalog no. AM9680; Ambion, Thermo Fisher Scientific) to mask unspecific binding, and 100 μg/mL of coprecipitant RNA (yeast RNA; catalog no. AM7118; Ambion). RNA probes were generated from human and mouse *APLN* and *APLNR* cDNA as described previously (15). The probe-containing hybridization solution was boiled at 95°C for 10 minutes before application. On day 2, nonspecific signals were removed by stringency washing in graded saline sodium citrate (from 20 × to 0.1 ×) and incubated with alkaline phosphatase–conjugated anti-DIG antibody (catalog no. 11093274910; Roche Diagnostics) overnight at 4°C. On day 3, the slides were washed in PBS-T (0.1% Tween in 1 × PBS) and incubated with 5-bromo-4-chloro-3-indolyl phosphate (BCIP)/nitro blue tetrazolium (NBT) substrate (catalog no. SK-5400; Vector Laboratories) in 0.1 mol/L Tris-HCl (pH 9.5) at 37°C for up to 4 days. For counterstaining with eosin, the slides underwent serial passages in graded alcohol (70%–100%) followed by application of Roti-Histol, and were then mounted with Entellan (catalog no. 107960, Merck Millipore). Pictures were taken under an Axioskop2 microscope with Axiocam 105 Color and Axiovision SE64 Rel. 4.9 software (Carl Zeiss). Quantification of pseudopalisading or apelin-positive areas was performed in ImageJ using the threshold function on six representative pictures (×5 magnification) per animal on hematoxylin and eosin (H&E) or on consecutive sections stained for apelin mRNA.

Immunofluorescence and vessel density quantification

Under pentobarbital (Narcoren; Merial) anesthesia, mice were transcardially perfused with 1× PBS followed by 4% phosphate-buffered PFA. The brain was postfixed for 2 days in 4% PFA and then left in 30% sucrose for ≥24 hours at 4°C. The brain was then embedded in Cryomatrix (catalog no. 6769006; Thermo Fisher Scientific) and frozen at −20°C. Tissue samples were prepared as horizontal sections (40-μm–thick) using a microtome. Floating sections were blocked for 1 hour at room temperature in 1× PBS containing 5% normal donkey serum (NDS; catalog no. 017-000-121; Jackson Immuno-Research), and 0.3% Triton-X (catalog no. 93418; Fluka). The sections were then incubated overnight at 4°C with the following primary antibodies: rabbit anti-MKi67 (1:200, catalog no. ab16667), rabbit anti-APLNR (1:100, catalog no. ab66218), rabbit anti-APLN 1:100, catalog no. ab59469 (all Abcam), rat anti-CD31 (1:50, catalog no. 550274; BD Biosciences), rabbit anti-von Willebrand factor (vWF; 1:400, catalog no. A0082; Dako, Agilent Technologies), or rabbit anti-GFP (1:500, catalog no. A11122; Thermo Fisher Scientific). The next day, the sections were incubated for 3 hours at room temperature with the following secondary antibodies: biotin-labeled donkey anti-rabbit or anti-rat antibody (1:250, catalog no. 711-065-152; 712-065-150) and/or 2 hours at room temperature with streptavidin-AF488 or -AF594 (1:500, catalog no. 016-540-084; 016-580-084, all Jackson Immuno-Research). Alternatively, sections were directly incubated for 2 hours at room temperature with the secondary antibodies donkey anti-rabbit AF488 or AF594 (1:500, catalog no. A-21206; A-21207, Thermo Fisher Scientific). All antibodies were diluted in blocking solution. For nuclear DAPI, 1:1,000 was used. After staining, tissue was mounted in fluorescent mounting medium (catalog no. S3023; Dako) and photographs were taken using an Axiovert25 microscope with Axiocam MRm and Axiovision Rel 4.8 software (Carl Zeiss).

Published OnlineFirst February 4, 2019; DOI: 10.1158/0008-5472.CAN-18-0881

Stereological analysis of vessel length density was performed for the GFP-positive tumor area of CD31- or vWF-positive red fluorescent vessels on every 12th section using the space ball method of StereoInvestigator Software 10.21.1 (MicroBrightField Bioscience) connected to an Olympus-BX53-microscope (Olympus Europe) and a motorized object table (MicroBrightField Bioscience).

IHC and tumor volume

Free-floating sections were immersed in 0.3% peroxide for 10 minutes to block endogenous peroxidase, washed in PBS, and incubated for 1 hour at room temperature in PBS containing 0.3% Triton X-100 and 5% NDS. Sections were then incubated with the primary antibodies rabbit anti-MKi67, rabbit anti-GFP (1:1,000, catalog no. A-11122, Thermo Fisher Scientific), or mouse anti-VIM (1:200, catalog no. sc-6260, Santa Cruz Biotechnology) overnight at 4°C in PBS containing 5% NDS. The next day, after three washes in PBS to remove unbound antibodies, the sections were incubated with secondary biotin donkey anti-rabbit, anti-rat, or anti-mouse antibodies (1:250, catalog no. 711-065-152; 712-065-150; 115-065-166, Jackson Immuno-Research) for 3 hours and then for 1 hour at room temperature with streptavidin-conjugated horseradish peroxidase (1:200, catalog no. SA-5004, Vector Laboratories). After washing in PBS, the sections were stained with DAB substrate according to the manufacturer's instructions (catalog no. DC137C100DCS, Innovative Diagnostik-Systeme). Finally, sections were mounted on glass slides (Superfrost Plus, R.Langenbrinck GmbH) and air dried for 10 minutes, followed by counterstaining with hematoxylin for 1 minutes. The slides were then rinsed with tap water, dehydrated with a graded series of ethanol (70%, 80%, 96%, 100%), cleared two times with xylene, and coverslipped with RotiHistokit II mounting medium (catalog no. 6640.1, Carl Roth GmbH). Tumor volumes were obtained from H&E or GFP-stained tumor sections by measuring the area of every 12th section and calculated using the Cavalieri method. The overall tumor volume was determined by measuring the total area including regions with single invasive tumor cells visible on GFP-stained sections. In addition, the compact tumor volume was determined by measuring the area of GFP-positive tumor cells that were in direct contact with neighboring tumor cells. The invasive tumor volume was determined as the difference between overall GFP and compact GFP tumor volume, and tumor invasiveness was determined as the percentage of invasive tumor volume over overall GFP tumor volume.

Statistical analysis

The distribution of each variable was summarized by its mean, SD, or SEM. Number of individuals, replicates, and or repetition of independent experiments are indicated in the figure text. In treatment groups comparing two groups, values are reported as the mean ± SD and unpaired Student *t* test was used to determine statistical significance. In treatment groups comparing more than two groups, values are reported as the mean ± SD and one-way ANOVA with Newman–Keuls *post hoc* test was used to determine statistical significance. For spheroid invasion assay, data are reported as the mean ± SEM and two-way ANOVA was used to determine the statistical significance. For survival experiments, Kaplan–Meier curves were used and log-rank (Mantel–Cox) test was applied to determine statistical significance. *P* values are indicated as *, $P < 0.05$; **, $P < 0.005$; and ***, $P < 0.0005$ in all results. All statistical analyses were conducted using GraphPad Prism 5.

Results

Apelin is downregulated by VEGFA/VEGFR2 blockade

We explored the pathophysiologic context of apelin signaling in a GBM subtype-specific manner by searching the TCGA dataset for genes coexpressed with *APLN* (the gene encoding for apelin; ref. 27). Interestingly, gene ontology analysis revealed that high apelin expression was associated with angiogenesis and blood vessel morphogenesis (Supplementary Fig. S1A) in the proneural or classical subtypes, but not in the mesenchymal subtype of GBM (Supplementary Table S1), which relates to previous observations that particularly the proneural and classical GBM subtypes may respond to antiangiogenic treatments (14, 28). To investigate a functional link between the VEGFA/VEGFR2 and apelin/APLNR signaling pathways, we examined the effects of bevacizumab in a mouse model of proneural GBM. First, we analyzed tumor samples from a murine platelet-derived growth factor B (PDGFB)-driven proneural-like GBM model based on the RCAS/Tva system (29). In this model, genetically manipulated NPCs are the point of origin for GBM. Tumor-bearing mice were then treated with a murine bevacizumab surrogate anti-VEGFA antibody (B20-4.1.1, Roche), which increased survival and decreased total vessel area, but also let to an increased tumor volume compared with mice treated with vehicle (30). *In situ* hybridization of control tumors revealed strong apelin mRNA expression in areas corresponding to GBM pseudopalisades (Fig. 1A asterisks) and tumor vessels (Fig. 1A arrows). In the anti-VEGFA antibody–treated samples, pseudopalisades were less prominently stained by apelin *in situ* hybridization (Fig. 1A asterisks) and smaller and less numerous vascular proliferates were detectable (Fig. 1A arrows). qPCR confirmed that apelin expression was downregulated in the treated samples as compared with control samples (Fig. 1A).

In a second set of experiments, we orthotopically implanted mice with murine transgenic GBM stem-like cells (GSCs; *p53* knockout GSCs overexpressing PDGFB, $p53^{KO}$PDGFB GSCs) as a model of human proneural GBM (31, 32). After tumor establishment, the murine VEGFR2-blocking antibody DC101 (corresponding to ramucirumab, Eli Lilly) was intracerebrally infused into the mice (Supplementary Fig. S1B). As in the RCAS/Tva model, the vehicle-treated control tumors showed strong apelin expression in tumor cells (Fig. 1B, asterisks) and in tumor vessels (Fig. 1B, arrows). Apelin mRNA expression was greatly reduced in the anti-VEGFR2–treated tumors. In particular, we found that apelin-labeling was strongly and significantly reduced in pseudopalisades within anti-VEGFR2–treated (5.1%) compared with control tumors (34.3%) while the extent of pseudopalisades (quantification of the total pseudopalisading area) was unchanged (Fig. 1C). Also *APLN*-positive vessel area was significantly reduced by 35% in anti-VEGFR2–treated tumors. Comparable observations were made in biopsies of GBM from patients before and after bevacizumab treatment. While the total area of pseudopalisading necrosis did not change (Fig. 1D; Supplementary Fig. S1C), we found that apelin expression was lower in the tumor samples obtained after antiangiogenic treatment (Fig. 1D; Supplementary

Published OnlineFirst February 4, 2019; DOI: 10.1158/0008-5472.CAN-18-0881

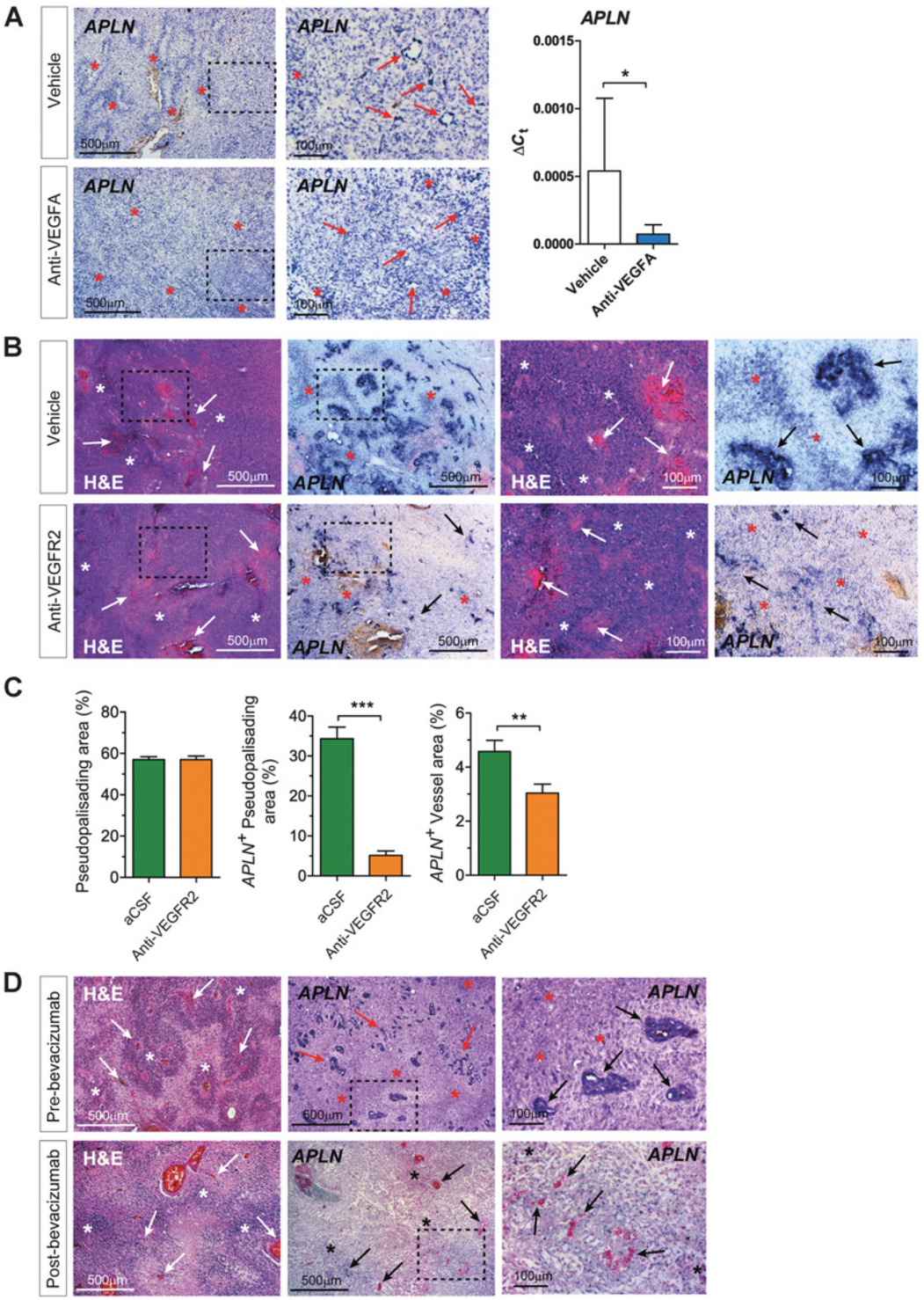

Figure 1.

Apelin is downregulated by anti-VEGFA or anti-VEGFR2 treatment. Mouse or human GBM samples were stained by H&E and consecutive sections were analyzed by *APLN in situ* hybridization; cell-dense pseudopalisading structures (asterisks) and vascular proliferates (arrows) are indicated. **A,** In a murine PDGFB-driven GBM model (RCAS/Tva system; ref. 29), apelin is strongly expressed in pseudopalisades and tumor vessels of controls (vehicle) but is weak in anti-VEGFA antibody-treated samples, with few apelin-positive vessels; this is corroborated by qPCR ($n = 4$ vs. 4). **B**, Mice orthotopically implanted with $p53^{KO}$PDGFB GSCs were intracerebrally infused with anti-VEGFR2 antibody or vehicle ($n = 7$ vs. 10). The overall extent of pseudopalisading structures was unchanged, but apelin levels were reduced in pseudopalisades and tumor vessels in anti-VEGFR2–treated tumors compared with controls. This was quantified in **C**. **D,** Biopsies from 7 patients pre- and post-bevacizumab were stained histologically and consecutive sections were inspected by *in situ* hybridization for apelin; note that apelin labeling is strong in vascular proliferates and pseudopalisades pre-bevacizumab but greatly reduced post-treatment. Scale size is indicated in individual micrographs; statistical significance (*t* test) is indicated. **, $P < 0.005$; ***, $P < 0.0005$.

Published OnlineFirst February 4, 2019; DOI: 10.1158/0008-5472.CAN-18-0881

Fig. S1D) than in the initial resected samples; note that control genes (e.g., *HPRT*, *ACTB*) were unchanged or upregulated (e.g., *NEK7*, *VAMP4*) confirming good RNA quality of patient samples (Supplementary Fig. S1D). In agreement with previous studies (15), we observed that apelin expression was also much higher in GBM (initial biopsy before antiangiogenesis) than in tumor-free human brain tissue (Supplementary Fig. S1E).

These results indicate that the *APLN* and *VEGFA* genes are coexpressed in GBM and that blocking VEGFA/VEGFR2 signaling with antibodies reduced apelin expression. Hence, we sought to

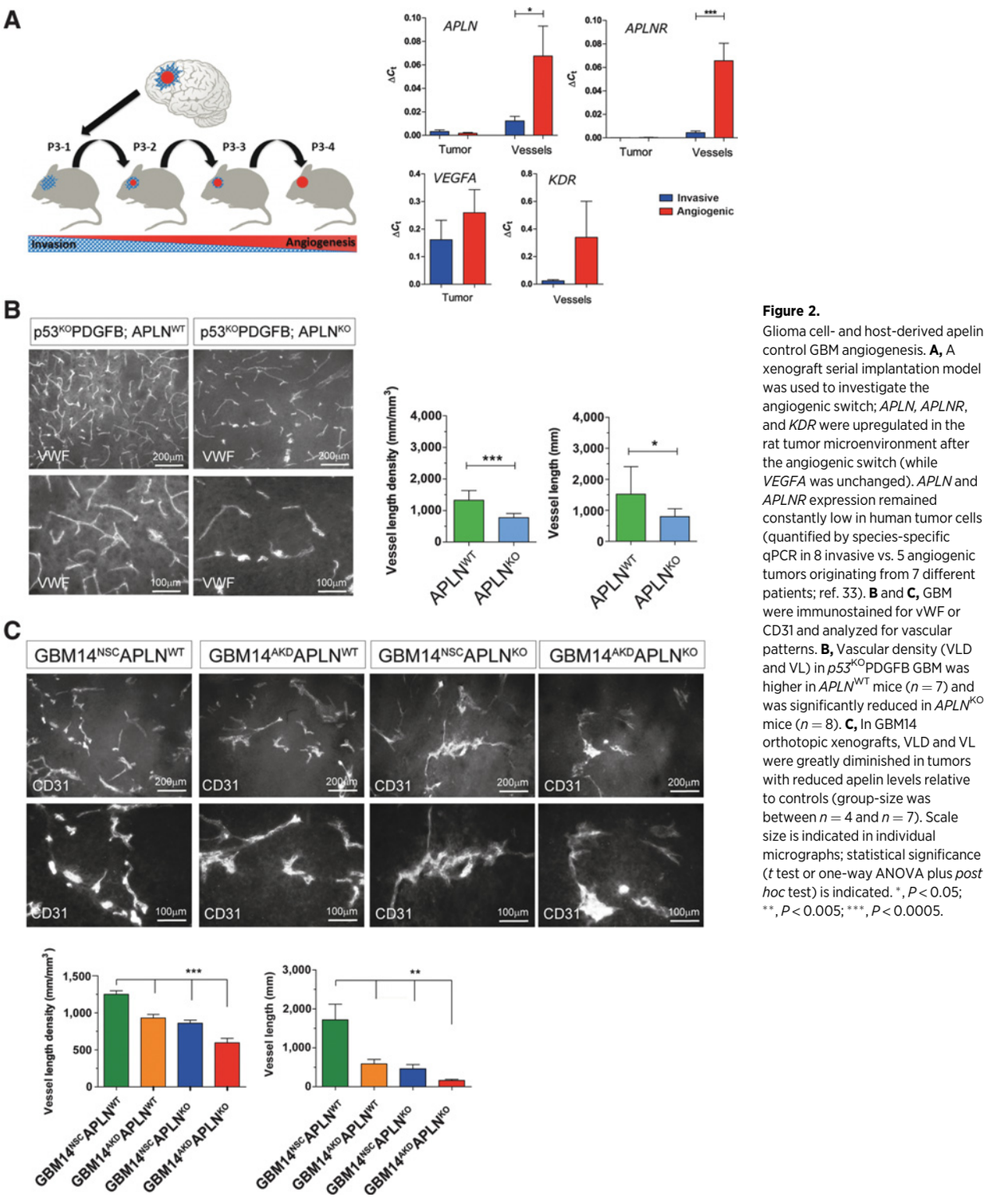

Figure 2.

Glioma cell- and host-derived apelin control GBM angiogenesis. **A,** A xenograft serial implantation model was used to investigate the angiogenic switch; *APLN, APLNR*, and *KDR* were upregulated in the rat tumor microenvironment after the angiogenic switch (while *VEGFA* was unchanged). *APLN* and *APLNR* expression remained constantly low in human tumor cells (quantified by species-specific qPCR in 8 invasive vs. 5 angiogenic tumors originating from 7 different patients; ref. 33). **B** and **C,** GBM were immunostained for vWF or CD31 and analyzed for vascular patterns. **B,** Vascular density (VLD and VL) in $p53^{KO}$PDGFB GBM was higher in $APLN^{WT}$ mice ($n = 7$) and was significantly reduced in $APLN^{KO}$ mice ($n = 8$). **C,** In GBM14 orthotopic xenografts, VLD and VL were greatly diminished in tumors with reduced apelin levels relative to controls (group-size was between $n = 4$ and $n = 7$). Scale size is indicated in individual micrographs; statistical significance (*t* test or one-way ANOVA plus *post hoc* test) is indicated. *, $P < 0.05$; **, $P < 0.005$; ***, $P < 0.0005$.

Published OnlineFirst February 4, 2019; DOI: 10.1158/0008-5472.CAN-18-0881

elucidate whether APLNR targeting has synergistic effects with VEGFA/VEGFR2 blockade. We also investigated the potential adverse effects of reduced apelin expression in GBM.

Apelin and APLNR upregulation is correlated with the angiogenic switch in GBM

We previously established a rodent model of the angiogenic switch in GBM that involved serial transplantation of a patient-derived xenograft (33–35). This model is initially characterized by highly infiltrative brain tumors without apparent neoangiogenesis (Fig. 2A; ref. 33), but after several generations of *in vivo* passaging acquires an angiogenic, noninvasive phenotype (angiogenic switch; ref. 34). This model (and an alternative model; ref. 35) allowed us to determine the relative expression levels of individual genes derived from the GBM cells or the host.

In both models, we compared the gene expression patterns in the initial generation of tumors against later-generation tumors (Fig. 2A). We found that the vascular expression levels of apelin and APLNR mRNA were dramatically increased in the tumor microenvironment of angiogenic versus invasive GBM (Fig. 2A; Supplementary Fig. S2A) highlighting a central role of the APLNR signaling pathway in promoting angiogenesis in GBM.

Host-derived apelin controls GBM angiogenesis

To study the role of APLNR signaling within the tumor microenvironment, we orthotopically implanted murine GSCs into *APLN*-wild-type ($APLN^{WT}$) or *APLN*-knockout ($APLN^{KO}$) mice. In the first set of *in vivo* experiments, we used proneural-like $p53^{KO}$PDGFB GSCs expressing low levels of apelin (Supplementary Fig. S2B). The GBM originating from these cells produced an invasive and well-vascularized tumor. The vessel length density (VLD) was quantified in the tumor area (1,327 mm/mm^3; Fig. 2B). When $p53^{KO}$PDGFB GSCs were implanted into $APLN^{KO}$ mice, the VLD was significantly reduced by 41% to 776 mm/mm^3. The intratumoral vessel length (VL) was reduced by 47% from 1,520 mm in $APLN^{WT}$ mice to 799 mm in $APLN^{KO}$ mice (Fig. 2B).

In human GBM, the apelin expression levels were related to angiogenic signaling pathways in proneural and classical, but not mesenchymal GBM. Therefore, we also established a mouse GSC culture model of the classical GBM subtype ($cdkn2a^{KO}$EGFRvIII GSCs; *CDKN2A*-knockout cells overexpressing EGFRvIII; refs. 28,

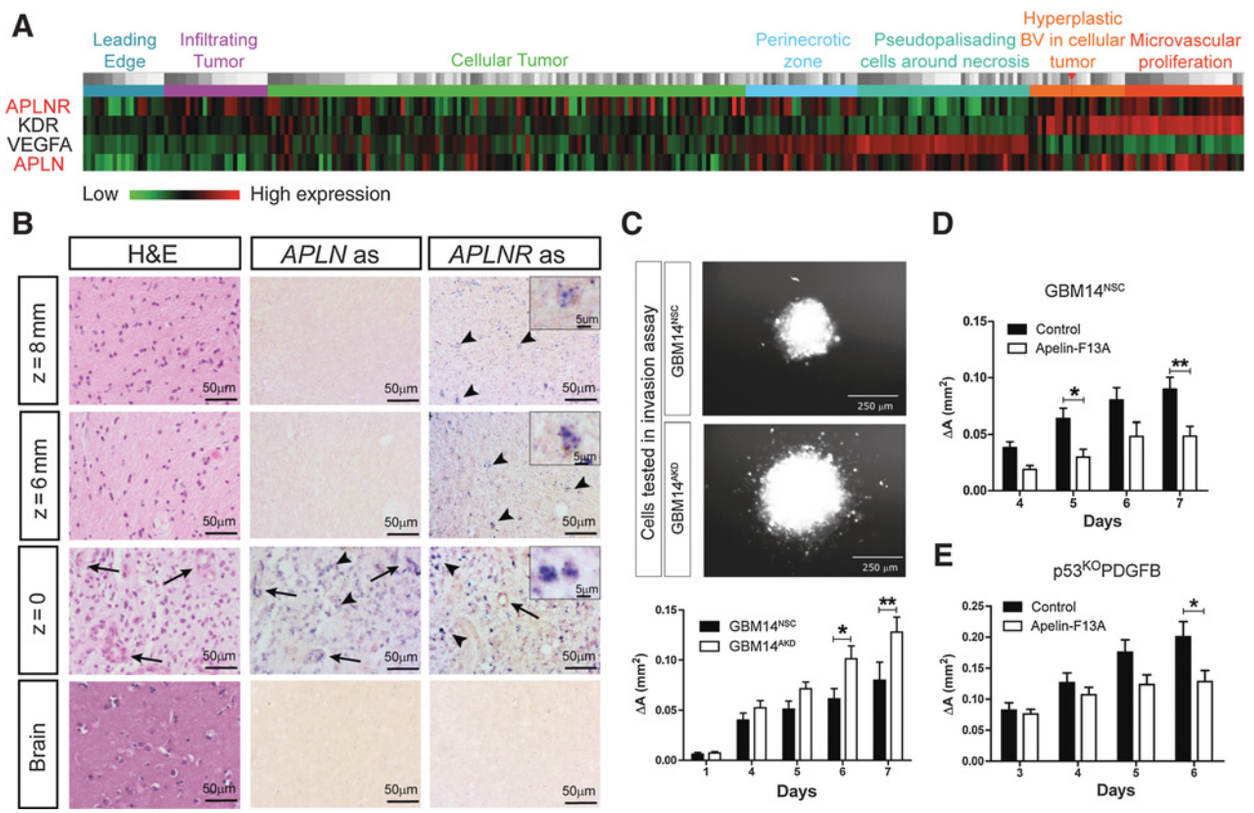

Figure 3.

APLNR is expressed in the tumor margin and attenuation of apelin/APLNR signaling *in vitro* uncovers a role of APLNR in GBM cell invasion. **A,** IVY GBM Atlas Project dataset depicting regional gene expression levels; note that *APLN* expression is high in pseudopalisades and *APLN* or *APLNR* are abundant in microvascular proliferations; *APLNR* alone is high in the infiltrating tumor area. **B,** Stereotactic GBM biopsies taken along a trajectory from the cell dense tumor (z = 0 mm) to the infiltrative tumor in the tumor periphery (z = 6 and 8 mm). *APLN* is expressed in tumor vessels (arrows) and individual cells (arrowheads) in the cell-dense tumor (z = 0), but is undetectable in the periphery (z = 6 and 8 mm). *APLNR* is expressed in tumor vessels (arrows) and in individual cells at z = 0, and in peripheral cells at z = 6 and 8 mm. The magnified insets show the cellular staining. *APLN* and *APLNR* are undetectable in tumor-free brain. **C**, *In vitro* spheroid invasion assay with $GBM14^{AKD}$ cells demonstrated significantly greater invasion compared with the control $GBM14^{NSC}$ cells. **D** and **E,** Application of 1 μmol/L of apelin-F13A attenuated invasion of $GBM14^{NSC}$ (**D**) and $p53^{KO}$PDGFB (**E**) GSCs. Data were obtained from at least five different spheres per condition. Scale size is indicated in individual micrographs; statistical significance (one-way ANOVA plus *post hoc* test) is indicated. *, $P < 0.05$; **, $P < 0.005$.

Published OnlineFirst February 4, 2019; DOI: 10.1158/0008-5472.CAN-18-0881

32). The GBM originating from *cdkn2a*^{KO}EGFRvIII GSCs produced a high vascular density (Supplementary Fig. S2C). The VLD was 2,746 mm/mm^3 in *APLN*^{WT} mice (Supplementary Fig. S2C) and was significantly reduced by 33% to 1,830 mm/mm^3 in *APLN*^{KO} mice. Overall vessel length (VL) was reduced by 75.4% from 82,726 mm in *APLN*^{WT} mice to 20,349 mm in *APLN*^{KO} mice. This set of experiments corroborated our working hypothesis that host-derived apelin plays a prominent role in controlling the extent of tumor vascularization.

Combined effects of GBM cell- and host-derived apelin on tumor angiogenesis

Next, we investigated the contribution of GBM cell–derived apelin on tumor angiogenesis *in vivo*. We selected two patient-derived GBM cultures of the proneural subtype that expressed relatively high levels of apelin (arrows in Supplementary Fig. S2D). First, we manipulated primary GBM14 cells (21) to express a shRNA construct to knockdown endogenous *APLN* (GBM14^{AKD}; Supplementary Fig. S2E) or a nonsilencing control shRNA (GBM14^{NSC}). *APLN*-knockdown (APLN^{KD} or AKD) did not affect GBM viability or expansion *in vitro* (Supplementary Fig. S2E). Six weeks after orthotopic injection of GBM14^{NSC} cells into immunocompromised wild-type mice, we detected the formation of a vascularized brain tumor mass with a VLD of 1,249 mm/mm^3 (Fig. 2C). The VLD of GBM14^{AKD} orthotopic xenografts in wild-type mice was 930 mm/mm^3, a reduction of 25.5% versus GBM14^{NSC}, which suggests that GBM-derived apelin is proangiogenic. The modulation of human GBM-derived apelin is pathologically meaningful in mouse models because the amino acid sequences of the bioactive peptide apelin-13 of human or mouse origin are identical (15).

Implantation of GBM14^{NSC} into *APLN*^{KO} mice reduced the tumor vasculature by approximately 25% as compared with GBM14^{NSC} gliomas grown in *APLN*^{WT} mice (Fig. 2C). When GBM14^{AKD} cells were implanted into immunodeficient *APLN*^{KO} mice, we detected scant tumor angiogenesis with a VLD of 569 mm/mm^3, a 54% reduction relative to that in control mice (Fig. 2C). Furthermore, the overall VL was reduced from 1,720 mm to 588 mm (by 66%), 460 mm (by 73%), and 161 mm (by 91%), respectively.

We also orthotopically implanted mice with a second well-established human primary GSC model (NCH644 cells (20)) corresponding to the proneural subtype (36). These cells produced a GBM with a VLD of 1,168 mm/mm^3 in wild-type mice (Supplementary Fig. S2F and S2G). Stable knockdown of *APLN* in the tumor cells (NCH644^{AKD}; Supplementary Fig. S2F) reduced the VLD by 50% to 648 mm/mm^3 (Supplementary Fig. S2G).

This series of experiments consistently indicated that tumor cell–derived and/or host-derived *APLN* levels are directly correlated with the level of tumor angiogenesis. GBM vascularization was reduced by *APLN* knockdown in tumor cells or *APLN* knockout. Injection of *APLN*^{KD} GBM cells into *APLN*^{KO} mice achieved an even greater reduction in GBM angiogenesis.

Reduced apelin in APLNR-expressing GBM is related to invasion

In the IVY Glioblastoma Atlas Project RNA-seq database, we found regionally distinct expression levels of apelin and APLNR (Fig. 3A; Supplementary Fig. S3A). In particular, apelin was more abundantly expressed in tumor areas enriched with microvascular proliferation and hyperplastic blood vessels (BV; with high levels of *KDR* expression). However, apelin expression was very low in microdissected GBM samples containing an infiltrating tumor or a leading edge (Fig. 3A), whereas APLNR mRNA expression remained high, especially in the infiltrating tumor zone (Fig. 3A). The elevated expression of APLNR was also associated with increased expression of genes involved in tumor cell invasion like *MMP2* (matrix metallopeptidase 2) and *BAI1/3* (brain-specific angiogenesis inhibitor 1/2), but the expression of tissue inhibitor of metalloproteinase-1 (TIMP1), an MMP2 inhibitor, was low (Supplementary Fig. S3A).

To further investigate a potential role of *APLNR* in invasive GBM areas, we used GBM biopsies obtained by neurosurgical resection using a neuronavigation system (Supplementary Fig. S3B). *In situ* hybridization revealed that the tumor center expressed apelin in cellular (arrowheads) and vascular regions (arrows; also visible on consecutive H&E), whereas apelin was not detected at the tumor border. APLNR was also expressed in the cellular (arrowheads) and vascular (arrows) regions in the tumor center, but APLNR expression was more pronounced in some dispersed cells along the tumor border (Supplementary Fig. S3B, arrowheads). To provide a greater resolution of local *APLN*/*APLNR* expression, we examined stereotactic GBM biopsies with defined three-dimensional coordinates (Fig. 3B). In successive biopsies taken along the stereotactic trajectory (*z*-axis), from the tumor core to the invasive zone, we observed a progressive reduction in apelin expression (Fig. 3B), but APLNR expression was maintained in individual cells (arrowheads) of the invasive margin. Also, immunostaining for APLNR in orthotopic GBM mouse models (see below) confirmed its expression in invasive tumor cells (Supplementary Fig. S3C and S3D). Taken together, these findings indicate that APLNR expression is maintained in scattered GBM cells within the apelin-free invasive tumor margin.

To investigate a potential role for apelin/APLNR signaling in GBM invasion *in vitro*, we embedded GBM14 cells (GBM14^{AKD} or GBM14^{NSC}) in a collagen matrix (28). We found that the GBM14^{AKD} cells were much more invasive than the control GBM14^{NSC} cells (Fig. 3C). To exclude that the increase in invasive area observed with GBM14^{AKD} cells compared with GBM14^{NSC} control cells was a result of enhanced proliferation we analyzed *in vitro* proliferation assays and compared their Ki67 status, but did not detect any differences (Supplementary Fig. S2E, S3E, and S3F).

Next by performing a wound healing and a Boyden chamber chemotaxis assay (Supplementary Fig. S3G and S3H), we confirmed that the depletion of apelin in GBM cells (GBM14 and U87MG) accelerates invasion *in vitro*. However, application of apelin-F13A, another APLNR ligand (37), to GBM14 spheres reduced invasiveness (Fig. 3D). A similar inhibitory effect of apelin-F13A on glioma cell invasion was also observed in murine *p53*^{KO}PDGFB GSCs (Fig. 3E). In line with that, addition of apelin-F13A in the two migration assays also attenuated the invasiveness of *APLN*^{KD} cells (Supplementary Fig. S3G–S3I).

Overall, we found that APLNR is expressed in the apelin-free invasive zone of patient-derived GBM samples, that the absence of endogenous apelin can increase GBM cell invasion *in vitro*, and that application of the APLNR ligand apelin-F13A has an anti-invasive effect.

Anti-invasive role of apelin in GBM *in vivo*

Next, we investigated whether apelin modulates tumor invasion in murine GBM models *in vivo*. Immunostaining for a GFP reporter in GBM14 cells and histologic staining revealed the

Published OnlineFirst February 4, 2019; DOI: 10.1158/0008-5472.CAN-18-0881

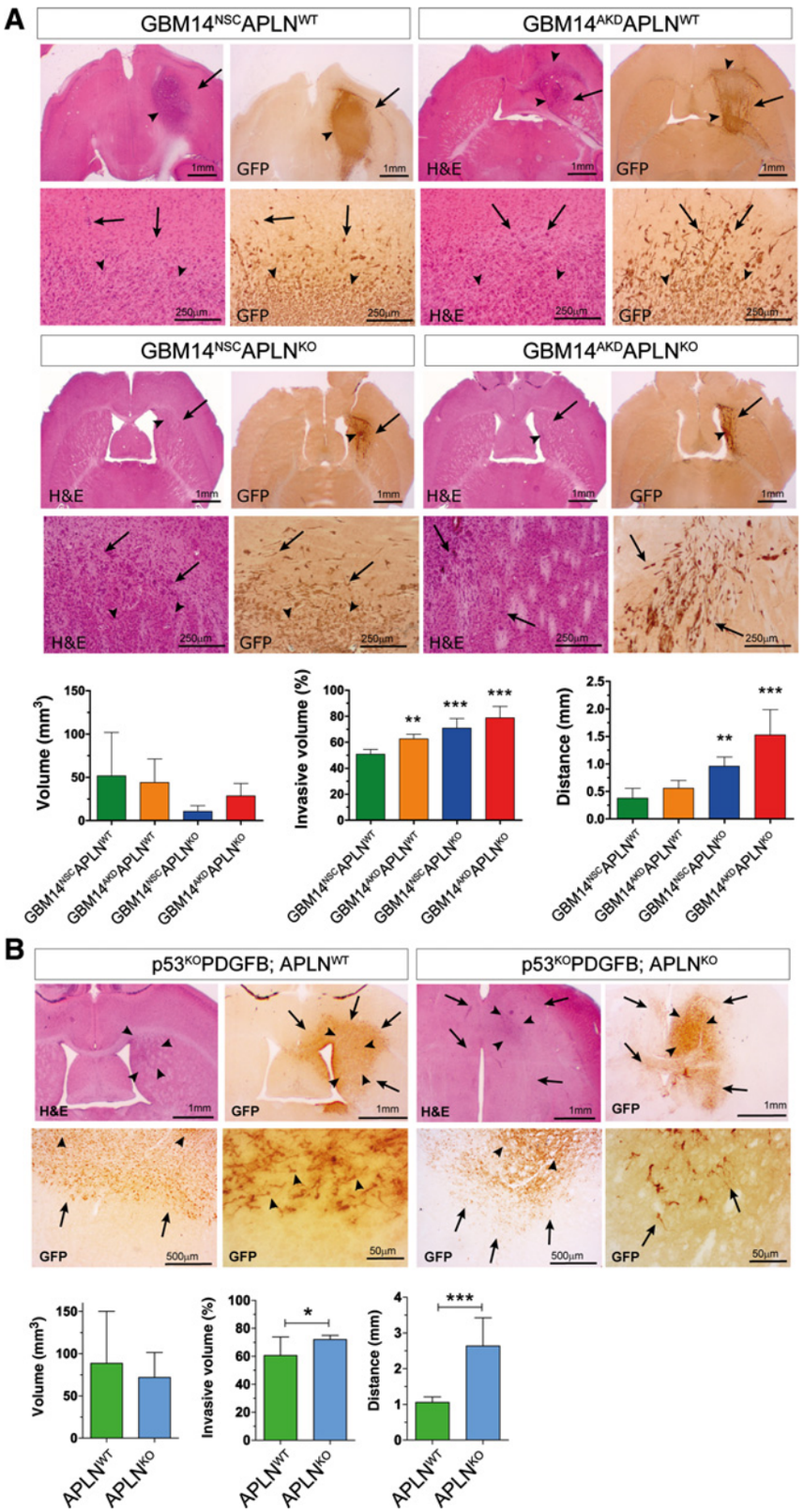

Figure 4.

Anti-invasive role of apelin in orthotopic models of proneural GBM. **A** and **B,** GBM were analyzed by H&E and GFP immunostaining to assess overall, compact, and invasive tumor volumes, as well as the migration distance of single cells from the tumor mass Arrowheads, compact tumor border; arrows, single invading cells. **A,** GBM14^{NSC} or GBM14^{AKD} GSCs were grown in immunodeficient *APLN*^{WT} or *APLN*^{KO} mice. Although there is no difference in overall tumor volume, the invasive tumor volume (% invasive volume) is significantly greater for GBM14^{AKD} cells implanted into *APLN*^{WT} ($n = 7$), GBM14^{NSC} cells implanted into *APLN*^{KO} ($n = 4$), and GBM14^{AKD} cells implanted into *APLN*^{KO} mice ($n = 4$) as compared with GBM14^{NSC} cells implanted into *APLN*^{WT} mice ($n = 7$). The distance of single invading cells to the tumor center is significantly greater in the *APLN*^{KO} mouse xenografts. **B,** *p53*^{KO}PDGFB GBM were grown in immunocompetent *APLN*^{WT} or *APLN*^{KO} mice. Although the overall tumor volume is unchanged in *APLN*^{KO} mice ($n = 8$) compared with *APLN*^{WT} mice ($n = 7$), the invasiveness, as assessed by percent invasive volume and distance of migration, is substantially increased in *APLN*^{KO} mice. Scale size is indicated in individual micrographs; statistical significance (*t* test or one-way ANOVA plus *post hoc* test) is indicated. *, $P < 0.05$; **, $P < 0.005$; ***, $P < 0.0005$.

Published OnlineFirst February 4, 2019; DOI: 10.1158/0008-5472.CAN-18-0881

tumor mass (H&E staining; Fig. 4A; arrowheads indicate compact GFP volume). In addition, individual GFP-positive cells (arrows) were observed to invade the brain. When intratumoral apelin levels were gradually reduced by implanting GBM14^{AKD} cells into *APLN*^{WT} mice, by inoculation of GBM14^{NSC} into *APLN*^{KO} animals or GBM14^{AKD} cells into *APLN*^{KO} mice, the overall tumor volume gradually decreased (as compared with controls), but the invasive volume of GBM cells increased significantly (Fig. 4A; Supplementary Fig. S4A).

We confirmed that the change of *in vivo* tumor volume was not a result of altered GBM cell proliferation (Supplementary Fig. S4B). Consistently, orthotopic implantation of NCH644^{NSC} GSCs generated tumors with few regions of accelerated invasiveness (Supplementary Fig. S4C, arrows), but implantation of NCH644^{AKD} cells resulted in a much more pronounced invasive pattern (Supplementary Fig. S4C, arrows).

Similar observations were made using an immunocompetent model of proneural GBM, in which we implanted *p53*^{KO}PDGFB GSCs into apelin-deficient hosts. Again, the resulting tumors were much more invasive than GBM grown in *APLN*^{WT} hosts (Fig. 4B). In *p53*^{KO}PDGFB GBM, the distance of tumor cell migration away from the dense tumor mass increased from 1.1 in *APLN*^{WT} to 2.6 mm in *APLN*^{KO} mice. In addition, the invasive ratio increased by 1.6 times (Supplementary Fig. S4D) and the percentage of invasive versus overall volume increased from 59% to 72% (Fig. 4B). Using *cdkn2a*^{KO}EGFRvIII GBM as a model of the classical subtype, we found that the compact and overall volumes were decreased by 53% in *APLN*^{KO} mice compared with *APLN*^{WT} mice, but tumor invasiveness significantly increased as well (Supplementary Fig. S4E).

In another approach to investigate apelin-modulated GBM cell invasion, we implanted human primary GBM cells into murine orthotopic brain slice cultures. Here apelin knockdown increased the invasiveness of proneural NCH644 as well as classical GBM5av cells (Supplementary Fig. S4F and S4G).

In summary, we found that apelin derived from the host and tumor cells is an essential mediator of neoangiogenesis in GBM and that apelin also contributes to suppressing GBM cell invasion. This was demonstrated by an inverse correlation between apelin expression levels with GBM invasiveness in our *in vitro*, *ex vivo*, and *in vivo* models and by the direct anti-invasive effect of APLNR stimulation in our collagen-based invasion as well as migration assays.

Apelin-F13A inhibits GBM angiogenesis and invasion

To study the potential of APLNR as a therapeutic target for GBM, we tested the *in vivo* application of apelin-F13A (37). Apelin-F13A with the C-terminal phenylalanine mutated to alanine can antagonize the APLNR *in vivo* (38), but was also found to act as an agonist on different functional assays, such as adenyl cyclase inhibition or APLNR internalization (39, 40). First, we established that APLNR is abundantly expressed in scattered, infiltrative GBM cells in our models (Supplementary Figs. S3C and S3D and S5A and S5B). Then we explored the therapeutic properties of apelin-F13A *in vivo*. We found that the vascular density of murine proneural-like GBM was reduced from a VLD of 1,069 mm/mm^3 in control mice to 629 mm/mm^3 in apelin-F13A–treated mice (Fig. 5A). The overall tumor volume was decreased by 56% from 104 mm^3 in control mice to 46 mm^3 in apelin-F13A–treated mice. While the compact tumor volume did not change significantly, the invasive tumor volume decreased by 53% from 72 mm^3 in control mice treated with artificial cerebrospinal fluid (aCSF) to 34 mm^3 in apelin-F13A–treated mice (Fig. 5A). We then repeated this experiment using proneural GBM14 GSCs. We observed a reduction in VLD for these human-derived GBM, from 1,333 mm/mm^3 in control mice to 749 mm/mm^3 in apelin-F13A–treated mice (Fig. 5B). In addition, overall tumor volume decreased by 68% from 69 mm^3 in control mice to 22 mm^3 in apelin-F13A–treated mice. As in the *p53*^{KO}PDGFB model, the compact tumor volume did not change significantly in the human GBM model, but the invasive tumor volume decreased by 59% from 31 mm^3 in control mice to 13 mm^3 in apelin-F13A–treated mice (Fig. 5B).

To test the binding specificity of the apelin peptides as well as the functional response of the GBM APLNR, we performed two *in vitro* internalization assays (15, 40–43); because internalization rates of GPCRs give valuable insight in signaling activity by native (nonrecombinant) GPCR (44). We found that the addition of apelin-13 and apelin-F13A caused the internalization of the APLNR to cytoplasmic and perinuclear regions (Supplementary Fig. S5C). Most interestingly, we detected a difference in the APLNR redistribution in response to the two peptides. While apelin-13 led to a massive decrease of APLNR localization in the nucleus, apelin-F13A caused exactly the opposite outcome (Supplementary Fig. S5C). In a second internalization assay, we administered GFP-linked apelin peptides to GBM14 cells. We found that both, apelin-13 and apelin-F13A, were internalized by the cells, while a scrambled peptide was not (Supplementary Fig. S5D). In addition, we confirmed the specificity of peptide uptake by performing a dose escalation with unlabeled peptide showing that uptake of both GFP-labeled peptides was specifically blocked by corresponding unlabeled peptides (Supplementary Fig. S5E).

These findings imply that the synthetic APLNR ligand apelin-F13A efficiently suppressed angiogenesis and invasiveness in two models of GBM (Fig. 6A). Apelin-F13A can bind and activate the APLNR, functions as a competitive agonist for other APLNR ligands, and has only partial APLNR-activating properties (19). Our receptor internalization assay revealed that apelin-13 or apelin-F13A induce distinct patterns of intracellular APLNR localization, which can point-out differences in signaling cues initiated by these two peptides. This may explain why only apelin-F13A (but not apelin-13) was able to block the proangiogenic effects of intratumoral apelin while both ligands suppressed tumor invasion (Supplementary Fig. S5F).

Cotargeting VEGFR2 and APLNR synergistically improved survival of murine models of GBM

One of the major adverse effects of bevacizumab for the treatment of GBM is an increase in tumor cell invasiveness or upregulation of alternative angiogenic factors (10). Hence, we asked whether blocking the proangiogenic and -invasive properties of APLNR could overcome the pathologic side effects of established antiangiogenic regimen like anti-VEGFR2 therapy, and hence improve overall survival. Orthotopically implanted *p53*^{KO}PDGFB GBM were allowed to expand for one week in mice. These mice were then treated intracerebrally with apelin-F13A, anti-VEGFR2 antibody, apelin-F13A, and anti-VEGFR2 antibody, or with vehicle (aCSF) alone as a control (Fig. 6B). The median survival of aCSF-treated mice was 52 days. Administration of anti-VEGFR2 increased survival by 28% compared with control mice, with a median survival of 67 days. Administration of apelin-F13A alone achieved a similar increase in survival (63 days; 19%

Published OnlineFirst February 4, 2019; DOI: 10.1158/0008-5472.CAN-18-0881

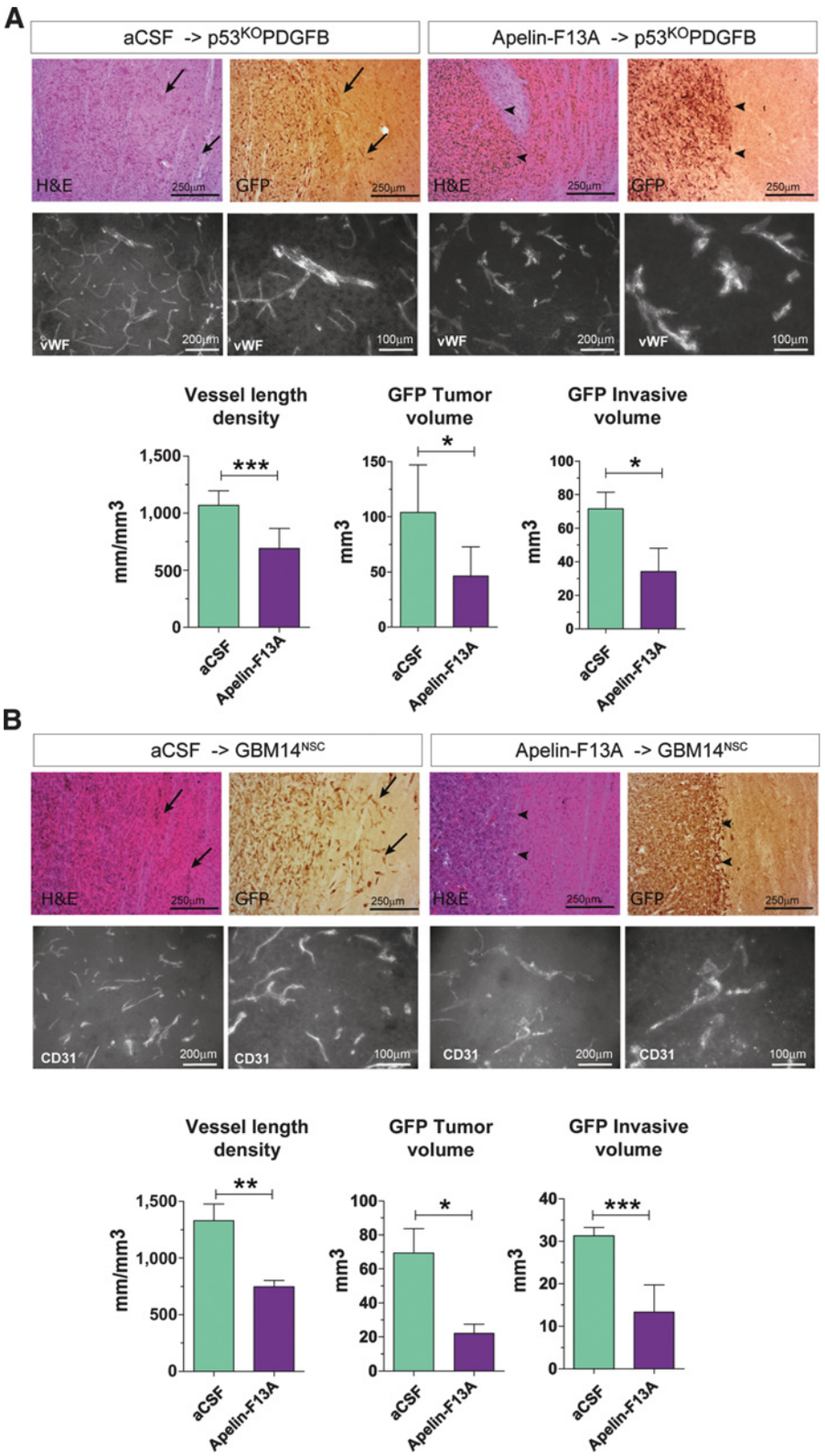

Figure 5.

The APLNR ligand apelin-F13A inhibits GBM angiogenesis and invasion. **A** and **B,** murine *p53*^{KO}PDGFB (**A**) or human GBM14 (**B**) GSCs were implanted and once GBM were established, aCSF or apelin-F13A was administered intracerebrally. Both, mouse- and patient-derived GBM showed a significant reduction in VLD and VL, as well as for invasive and overall tumor volume. Arrows, single invasive tumor cells in GFP- or H&E-stained sections; arrowheads, compact tumor border. aCSF or apelin-F13A were infused into 8 and 6 mice with murine GBM and 6 and 5 mice with human GBM, respectively. Scale size is indicated in individual micrographs; statistical significance (*t* test) is indicated. *, $P < 0.05$; **, $P < 0.005$; ***, $P < 0.0005$.

Published OnlineFirst February 4, 2019; DOI: 10.1158/0008-5472.CAN-18-0881

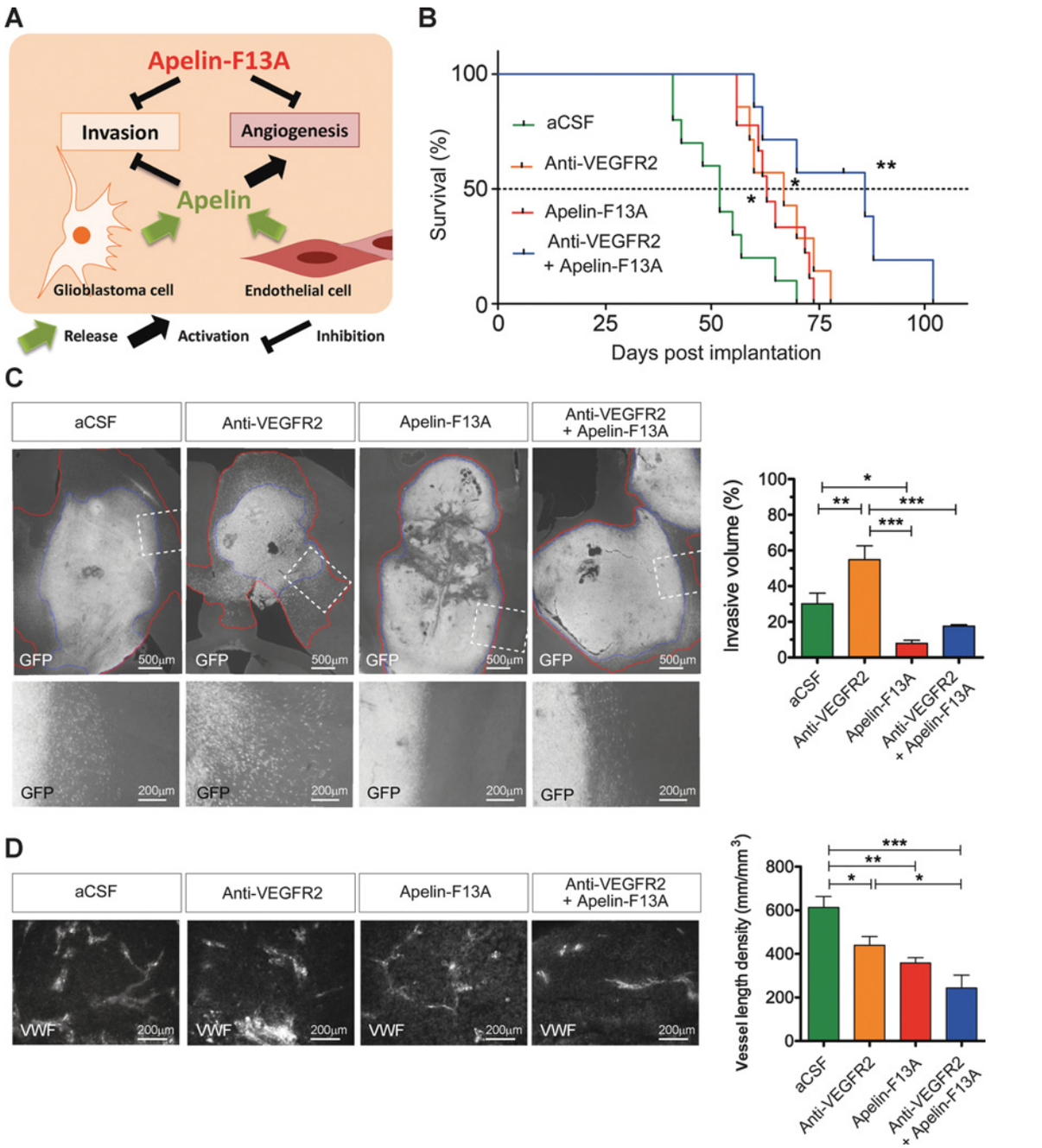

Figure 6.

Cotargeting of VEGFR2 and APLNR synergistically improves survival of mice bearing GBM. **A,** Model for apelin/APLNR signaling in GBM. Apelin is released by GBM and/or endothelial cells, activates APLNR on tumor cells (which inhibits invasion) and on endothelia (activating/sustaining angiogenesis); administration of apelin-F13A attenuates both angiogenesis and invasion. **B,** Intracerebral infusion of apelin-F13A and/or anti-VEGFR2 antibody significantly increased survival compared with the infusion of aCSF in mice bearing $p53^{KO}$PDGFB GBM. Cotreatment with apelin-F13A and anti-VEGFR2 increased survival by additional 28% ($P < 0.05$) compared with anti-VEGFR2 single treatment. Ten, 7, 9, and 6 mice were treated with aCSF, anti-VEGFR2, apelin-F13A, and anti-VEGFR2 plus apelin-F13A, respectively. **C,** GBM invasiveness was analyzed in GFP-stained sections. In the composite images, the compact border (blue line) and the invasive tumor border (red line) are indicated. In the magnified images, massive invasion of single cells is visible in anti-VEGFR2–treated tumors. While the invasive GBM volume increased in anti-VEGFR2–treated tumors compared with control tumors, the invasive GBM volume was decreased in apelin-F13A-treated and anti-VEGFR2 and apelin-F13A cotreated mice. Data are shown for 4 and 5 tumors for treated versus control group. **D,** VEGFR2 and apelin-F13 treatment significantly decreased VLD to 440 and 357 mm/mm^3, respectively, versus 613 mm/mm^3 in control mice. Coadministration of anti-VEGFR2 and apelin-F13 decreased VLD to 243 mm/mm^3, which was significantly lower than that in anti-VEGFR2–treated tumors. Four tumors were analyzed per group. Scale size is indicated in individual micrographs; statistical significance (one-way ANOVA plus *post hoc* test) is indicated. *, $P < 0.05$; **, $P < 0.005$; ***, $P < 0.0005$.

Published OnlineFirst February 4, 2019; DOI: 10.1158/0008-5472.CAN-18-0881

increase) compared with control mice. Notably, coadministration of anti-VEGFR2 and apelin-F13A had synergistic effects, with a 65% increase in the survival rate (86 days). Median survival of the cotreated mice was significantly improved compared with administration of anti-VEGFR2 ($P = 0.0385$) or apelin-F13A ($P = 0.0327$) alone. Immunohistologic analysis of tumors with comparable overall tumor volume showed that administration of anti-VEGFR2 alone had a proinvasive effect with a 77% increase in the invasive volume relative to control mice (Fig. 6C). Interestingly, the anti-invasive effect of apelin-F13A reduced the invasive volume by 74 % significantly compared with control mice and combined treatment by 66% compared with anti-VEGFR2 treatment alone. Anti-VEGFR2 decreased VLD to 72% and apelin-F13A decreased VLD to 58% relative to control mice (Fig. 6D), while coadministration of apelin-F13A and anti-VEGFR2 decreased the VLD to 40% compared with controls.

In summary, we observed that cotargeting of the APLNR and VEGFR2 signaling pathways exerted synergistic antiangiogenic effects and strongly reduced the proinvasive side effects of established antiangiogenic strategies. We suggest that inhibition of VEGFR2 may be beneficial for the treatment of patients with the proneural subtype of GBM, if apelin-F13A is coadministered to modulate APLNR activation.

Discussion

In this study, we revealed a central role of the apelin/APLNR signaling pathway in antiangiogenic treatment of GBM and in countering resistance to bevacizumab. We showed that apelin is required for tumor angiogenesis and we uncovered a previously unknown function of the apelin/APLNR signaling pathway in GBM cell invasion (Fig. 6A). Furthermore, we investigated for the first time the pathologic roles of host- or tumor cell–derived apelin separately, and examined their specific effects on GBM expansion, invasion, and angiogenesis. Our data indicate that the apelin/APLNR signaling pathway has dichotomous roles in angiogenesis and invasion in GBM, and we established that stimulation of APLNR using apelin-F13A is a promising strategy to treat distinct subtypes of GBM. A clinical perspective for the coapplication of apelin-F13A together with VEGFA/VEGFR2 inhibitors is also suggested because coadministration of apelin-F13A and DC101 synergistically blunted GBM vascularization and diminished the proinvasive side-effects associated with VEGFA/VEGFR2 inhibition. In addition, the reduced vascularization might be accompanied with vascular normalization that could be supportive for combined chemotherapy (18).

In previous studies, the pathologic function of apelin was largely associated with tumor vascularization (45–47) and consequently we observed that tumor cell- and host-derived apelin has additive effects on tumor angiogenesis. We found that apelin expression levels were positively correlated with vascular density in murine and human GBM models of the proneural GBM subtype as well as in classical GBM. The vascular upregulation of apelin was further confirmed by colocalization of apelin peptide in tumor vessels by immunofluorescence (Supplementary Fig. S6). We focused on the proneural and classical subtypes of GBM because TCGA data suggested that the apelin/APLNR signaling pathway mediates vascularization in these two subtypes, but not in the mesenchymal subtype of GBM.

In this study, we used GSC cultures that were previously extensively characterized for their stem-like capacity (22, 48). A recent publication proposed a critical role of the apelin/APLNR signaling pathway in GSC maintenance (49). However, in our GSC models, we did not find any alterations in cell viability, proliferation, or sphere formation capability following attenuation of apelin expression or APLNR blockade.

Knockdown of *APLN* in GBM cells or knockout of *APLN* in the host both enhanced tumor cell invasion, and implantation of $APLN^{KD}$ cells into $APLN^{KO}$ mice further accelerated the dissemination of GBM cells. This was particularly apparent in GBM cells with elevated APLNR expression levels. Application of apelin-F13A blunted GBM invasion and neoangiogenesis. These findings support the view that autocrine and paracrine apelin signaling has proangiogenic effects on vascular cells and blunts invasion of GBM cells (Fig. 6A). This observation is clinically relevant because bevacizumab lowers intratumoral apelin levels, which may explain why bevacizumab-treated patients often suffer from increased GBM cell invasion (10). We propose that bevacizumab directly (via blockade of VEGFA activity) and indirectly (by lowering apelin expression) exerts powerful antiangiogenic effects. However, we have shown that a reduction in apelin disinhibits GBM cell invasion, which may result in treatment resistance. Our data suggest that the synthetic APLNR ligand apelin-F13A can support antiangiogenic therapies by blocking vascularization (synergistically with VEGFA/VEGFR2 inhibitors) and preventing invasion. In this study, we exploited the pharmacologic properties of apelin-F13A, which acts as a partial agonist for APLNR (19, 50) and as a competitive agonist for natural apelin isoforms, like apelin-13 (37). We hypothesize that apelin-F13A cannot sufficiently activate APLNR expressed on the endothelium to induce vascular sprouting but sufficiently stimulates APLNR on GBM cells to blunt invasion and prolong survival. This can be explained by a lower receptor binding capacity (39) and alternative activation of intracellular signaling pathways (51) by apelin-F13A as compared with natural APLNR ligands. Although we could not formally show direct binding of apelin-F13A on tumor endothelial cells *in vivo*, most recent findings of Zhao and colleagues (52) are in full support of our results by demonstrating apelin-F13A binding to APLNR in a structural *in silico* model and showing antiangiogenic effects of apelin-F13A on APLNR-expressing endothelia in peripheral tumors. We acknowledge that the experimental therapeutic agent apelin-F13A may have further effects on the tumor microenvironment (like, for example, on intratumoural immune cell populations), which could support the antiangiogenic and anti-invasive traits reported here. However, when we quantified tumor-associated myeloid cells in experimental GBM treated with vehicle or apelin-F13A we did not observe a difference in myeloid cell numbers.

Clinical trials of GBM therapies in the last two decades have highlighted the need to identify predictive markers to improve the clinical outcomes of new compounds (2, 53). One approach for patient stratification according to molecular and pathologic criteria involves clustering of GBM into genetic subtypes (12), which may be particularly relevant to antiangiogenic treatments using bevacizumab (14) and apelin-F13A (as in this study) because both agents have beneficial effects on the proneural subtype of GBM. In addition, the high expression of APLNR in GBM may qualify as a marker for an increased propensity of GBM cells to invade during bevacizumab treatment, a process that can be blocked by apelin-F13A.

Published OnlineFirst February 4, 2019; DOI: 10.1158/0008-5472.CAN-18-0881

In conclusion, the results of this study introduce a new strategy to reduce therapeutic resistance during antiangiogenic therapy and identify GBM subtypes that may show better therapeutic responses by cotargeting the apelin/APLNR and VEGFA/VEGFR2 signaling pathways.

Disclosure of Potential Conflicts of Interest

A.L. Vescovi is a CEO at Stemgen SpA, is a CEO and CSO at Hyperstem SA, and has ownership interest (including stock, patents, etc.) in Hyperstem SA. No potential conflicts of interest were disclosed by the other authors.

Authors' Contributions

Conception and design: G. Mastrella, V.M. Stoecklein, M. Synowitz, R. Glass, R.E. Kälin

Development of methodology: G. Mastrella, M. Synowitz, E. Wagner, R. Bjerkvig, R.E. Kälin

Acquisition of data (provided animals, acquired and managed patients, provided facilities, etc.): G. Mastrella, M. Hou, M. Li, V.M. Stoecklein, N. Zdouc, M.N.M. Volmar, H. Miletic, C.C. Herold-Mende, K. Eisenhut, P.N. Harter, E. Wagner, M. Mittelbronn, R. Bjerkvig, D. Hambardzumyan, U. Schüller, J. Radke, R. Glass, R.E. Kälin

Analysis and interpretation of data (e.g., statistical analysis, biostatistics, computational analysis): G. Mastrella, M. Hou, M. Li, V.M. Stoecklein, N. Zdouc, S. Reinhard, M. Synowitz, A.L. Vescovi, P.N. Harter, M. Mittelbronn, R. Bjerkvig, J. Radke, R. Glass, R.E. Kälin

Writing, review, and/or revision of the manuscript: G. Mastrella, M. Li, V.M. Stoecklein, M.N.M. Volmar, S. Reinhard, C.C. Herold-Mende, G. Gargiulo, M. Synowitz, P.N. Harter, E. Wagner, M. Mittelbronn, D. Hambardzumyan, U. Schüller, J.-C. Tonn, J. Radke, R. Glass, R.E. Kälin

Administrative, technical, or material support (i.e., reporting or organizing data, constructing databases): M. Li, S. Reinhard, S. Kleber, G. Gargiulo, J.M. Penninger, M. Mittelbronn, U. Schüller, R. Glass, R.E. Kälin

Study supervision: R. Glass, R.E. Kälin

Other (established and provided HGBM cancer stem cell line): A.L. Vescovi

Acknowledgments

R. Glass and R.E. Kälin gratefully acknowledge funding by the DFG (GL691/2; SFB824), the "Wilhelm Sander-Stiftung," the "Anni-Hofmann Stiftung," the "Verein zur Förderung von Wissenschaft und Forschung an der Medizinischen Fakultät der LMU München" (WiFoMed), the Curt Bohnewandt Fonds, the "Friedrich-Baur-Stiftung," and the "Familie Mehdorn Stiftung." M. Li was supported by a China Scholarship Council (CSC) graduate scholarship. J. Radke is a participant in the BIH-Charité Clinical Scientist Program funded by the Charité-Universitätsmedizin Berlin and the Berlin Institute of Health. U. Schüller is supported by the "Fördergemeinschaft Kinderkrebs-Zentrum Hamburg". M. Mittelbronn would like to thank the Luxembourg National Research Fond (FNR) for the support (FNR PEARL P16/BM/11192868 grant). We are thankful to Frank L. Heppner, Stefanie Lange, Eva Sušnik, Eskil Eskilsson, Per Øystein Sakariassen, as well as Steffen Dietzel and Andreas Thomae (Core Facility Bioimaging, Biomedical Center, LMU München), Günter Höglinger, Sigrid Schwarz, and Nicholas D. Smith (http://www.scientific-writing.net/).

The costs of publication of this article were defrayed in part by the payment of page charges. This article must therefore be hereby marked *advertisement* in accordance with 18 U.S.C. Section 1734 solely to indicate this fact.

Received March 22, 2018; revised October 19, 2018; accepted January 29, 2019; published first February 4, 2019.

References

1. Louis DN, Perry A, Reifenberger G, von Deimling A, Figarella-Branger D, Cavenee WK, et al. The 2016 world health organization classification of tumors of the central nervous system: a summary. Acta Neuropathol 2016;131:803–20.
2. Stupp R, Mason WP, van den Bent MJ, Weller M, Fisher B, Taphoorn MJ, et al. Radiotherapy plus concomitant and adjuvant temozolomide for glioblastoma. N Engl J Med 2005;352:987–96.
3. Weller M, van den Bent M, Tonn JC, Stupp R, Preusser M, Cohen-Jonathan-Moyal E, et al. European Association for Neuro-Oncology (EANO) guideline on the diagnosis and treatment of adult astrocytic and oligodendroglial gliomas. Lancet Oncol 2017;18:e315–e29.
4. Brennan CW, Verhaak RG, McKenna A, Campos B, Noushmehr H, Salama SR, et al. The somatic genomic landscape of glioblastoma. Cell 2013;155:462–77.
5. Chen J, McKay RM, Parada LF. Malignant glioma: lessons from genomics, mouse models, and stem cells. Cell 2012;149:36–47.
6. Westphal M, Lamszus K. The neurobiology of gliomas: from cell biology to the development of therapeutic approaches. Nat Rev Neurosci 2011;12:495–508.
7. Jain RK, di Tomaso E, Duda DG, Loeffler JS, Sorensen AG, Batchelor TT. Angiogenesis in brain tumours. Nat Rev Neurosci 2007;8:610–22.
8. Chinot OL, Wick W, Mason W, Henriksson R, Saran F, Nishikawa R, et al. Bevacizumab plus radiotherapy-temozolomide for newly diagnosed glioblastoma. N Engl J Med 2014;370:709–22.
9. Gilbert MR, Dignam JJ, Armstrong TS, Wefel JS, Blumenthal DT, Vogelbaum MA, et al. A randomized trial of bevacizumab for newly diagnosed glioblastoma. N Engl J Med 2014;370:699–708.
10. Lu KV, Bergers G. Mechanisms of evasive resistance to anti-VEGF therapy in glioblastoma. CNS Oncol 2013;2:49–65.
11. Aldape K, Zadeh G, Mansouri S, Reifenberger G, von Deimling A. Glioblastoma: pathology, molecular mechanisms and markers. Acta Neuropathol 2015;129:829–48.
12. Verhaak RG, Hoadley KA, Purdom E, Wang V, Qi Y, Wilkerson MD, et al. Integrated genomic analysis identifies clinically relevant subtypes of glioblastoma characterized by abnormalities in PDGFRA, IDH1, EGFR, and NF1. Cancer Cell 2010;17:98–110.
13. Wang Q, Hu B, Hu X, Kim H, Squatrito M, Scarpace L, et al. Tumor evolution of glioma-intrinsic gene expression subtypes associates with immunological changes in the microenvironment. Cancer Cell 2017;32:42–56.
14. Sandmann T, Bourgon R, Garcia J, Li C, Cloughesy T, Chinot OL, et al. Patients with proneural glioblastoma may derive overall survival benefit from the addition of bevacizumab to first-line radiotherapy and temozolomide: retrospective analysis of the AVAglio Trial. J Clin Oncol 2015;33:2735–44.
15. Kälin RE, Kretz MP, Meyer AM, Kispert A, Heppner FL, Brändli AW. Paracrine and autocrine mechanisms of apelin signaling govern embryonic and tumor angiogenesis. Dev Biol 2007;305:599–614.
16. Plate KH, Breier G, Weich HA, Risau W. Vascular endothelial growth factor is a potential tumour angiogenesis factor in human gliomas in vivo. Nature 1992;359:845–8.
17. Kälin S, Kälin RE. Apelin and cancer. In: Reizes O, Berger NA, editors. Adipocitokines, energy balance, and cancer. Basel, Switzerland: Springer International Publishing; 2017. p 137–66.
18. Zhang L, Takara K, Yamakawa D, Kidoya H, Takakura N. Apelin as a marker for monitoring the tumor vessel normalization window during antiangiogenic therapy. Cancer Sci 2016;107:36–44.
19. O'Carroll AM, Lolait SJ, Harris LE, Pope GR. The apelin receptor APJ: journey from an orphan to a multifaceted regulator of homeostasis. J Endocrinol 2013;219:R13–35.
20. Campos B, Wan F, Farhadi M, Ernst A, Zeppernick F, Tagscherer KE, et al. Differentiation therapy exerts antitumor effects on stem-like glioma cells. Clin Cancer Res 2010;16:2715–28.
21. Drachsler M, Kleber S, Mateos A, Volk K, Mohr N, Chen S, et al. CD95 maintains stem cell-like and non-classical EMT programs in primary human glioblastoma cells. Cell Death Dis 2016;7:e2209.
22. Binda E, Visioli A, Giani F, Trivieri N, Palumbo O, Restelli S, et al. Wnt5a Drives an invasive phenotype in human glioblastoma stem-like cells. Cancer Res 2017;77:996–1007.
23. UKCCCR guidelines for the welfare of animals in experimental neoplasia. Cancer Metastasis Rev 1989;8:82–8.

Published OnlineFirst February 4, 2019; DOI: 10.1158/0008-5472.CAN-18-0881

24. Kuba K, Zhang L, Imai Y, Arab S, Chen M, Maekawa Y, et al. Impaired heart contractility in Apelin gene-deficient mice associated with aging and pressure overload. Circ Res 2007;101:e32–42.
25. Shinkai Y, Rathbun G, Lam KP, Oltz EM, Stewart V, Mendelsohn M, et al. RAG-2-deficient mice lack mature lymphocytes owing to inability to initiate V(D)J rearrangement. Cell 1992;68:855–67.
26. Grathwohl SA, Kälin RE, Bolmont T, Prokop S, Winkelmann G, Kaeser SA, et al. Formation and maintenance of Alzheimer's disease beta-amyloid plaques in the absence of microglia. Nat Neurosci 2009;12:1361–3.
27. Bowman RL, Wang Q, Carro A, Verhaak RG, Squatrito M. GlioVis data portal for visualization and analysis of brain tumor expression datasets. Neuro Oncol 2017;19:139–41.
28. Eskilsson E, Rosland GV, Talasila KM, Knappskog S, Keunen O, Sottoriva A, et al. EGFRvIII mutations can emerge as late and heterogenous events in glioblastoma development and promote angiogenesis through Src activation. Neuro Oncol 2016;18:1644–55.
29. Hambardzumyan D, Amankulor NM, Helmy KY, Becher OJ, Holland EC. Modeling adult gliomas using RCAS/t-va technology. Transl Oncol 2009;2:89–95.
30. Pitter KL, Tamagno I, Alikhanyan K, Hosni-Ahmed A, Pattwell SS, Donnola S, et al. Corticosteroids compromise survival in glioblastoma. Brain 2016;139:1458–71.
31. Sonabend AM, Yun J, Lei L, Leung R, Soderquist C, Crisman C, et al. Murine cell line model of proneural glioma for evaluation of anti-tumor therapies. J Neurooncol 2013;112:375–82.
32. Jones TS, Holland EC. Animal models for glioma drug discovery. Expert Opin Drug Discov 2011;6:1271–83.
33. Sakariassen PO, Prestegarden L, Wang J, Skaftnesmo KO, Mahesparan R, Molthoff C, et al. Angiogenesis-independent tumor growth mediated by stem-like cancer cells. Proc Natl Acad Sci U S A 2006;103:16466–71.
34. Keunen O, Johansson M, Oudin A, Sanzey M, Rahim SA, Fack F, et al. Anti-VEGF treatment reduces blood supply and increases tumor cell invasion in glioblastoma. Proc Natl Acad Sci U S A 2011;108:3749–54.
35. Talasila KM, Soentgerath A, Euskirchen P, Rosland GV, Wang J, Huszthy PC, et al. EGFR wild-type amplification and activation promote invasion and development of glioblastoma independent of angiogenesis. Acta Neuropathol 2013;125:683–98.
36. Podergajs N, Brekka N, Radlwimmer B, Herold-Mende C, Talasila KM, Tiemann K, et al. Expansive growth of two glioblastoma stem-like cell lines is mediated by bFGF and not by EGF. Radiol Oncol 2013;47:330–7.
37. Lee DK, George SR, O'Dowd BF. Unravelling the roles of the apelin system: prospective therapeutic applications in heart failure and obesity. Trends Pharmacol Sci 2006;27:190–4.
38. Lee DK, Saldivia VR, Nguyen T, Cheng R, George SR, O'Dowd BF. Modification of the terminal residue of apelin-13 antagonizes its hypotensive action. Endocrinology 2005;146:231–6.
39. Medhurst AD, Jennings CA, Robbins MJ, Davis RP, Ellis C, Winborn KY, et al. Pharmacological and immunohistochemical characterization of the APJ receptor and its endogenous ligand apelin. J Neurochem 2003;84:1162–72.
40. Fan X, Zhou N, Zhang X, Mukhtar M, Lu Z, Fang J, et al. Structural and functional study of the apelin-13 peptide, an endogenous ligand of the HIV-1 coreceptor, APJ. Biochemistry 2003;42:10163–8.
41. Pope GR, Tilve S, McArdle CA, Lolait SJ, O'Carroll AM. Agonist-induced internalization and desensitization of the apelin receptor. Mol Cell Endocrinol 2016;437:108–19.
42. Reaux A, De Mota N, Skultetyova I, Lenkei Z, El Messari S, Gallatz K, et al. Physiological role of a novel neuropeptide, apelin, and its receptor in the rat brain. J Neurochem 2001;77:1085–96.
43. Zou MX, Liu HY, Haraguchi Y, Soda Y, Tatemoto K, Hoshino H. Apelin peptides block the entry of human immunodeficiency virus (HIV). FEBS Lett 2000;473:15–8.
44. Calebiro D, Godbole A. Internalization of G-protein-coupled receptors: Implication in receptor function, physiology and diseases. Best Pract Res Clin Endocrinol Metab 2018;32:83–91.
45. Berta J, Hoda MA, Laszlo V, Rozsas A, Garay T, Torok S, et al. Apelin promotes lymphangiogenesis and lymph node metastasis. Oncotarget 2014;5:4426–37.
46. Berta J, Kenessey I, Dobos J, Tovari J, Klepetko W, Jan Ankersmit H, et al. Apelin expression in human non-small cell lung cancer: role in angiogenesis and prognosis. J Thorac Oncol 2010;5:1120–9.
47. Sorli SC, Le Gonidec S, Knibiehler B, Audigier Y. Apelin is a potent activator of tumour neoangiogenesis. Oncogene 2007;26:7692–9.
48. Podergajs N, Motaln H, Rajcevic U, Verbovsek U, Korsic M, Obad N, et al. Transmembrane protein CD9 is glioblastoma biomarker, relevant for maintenance of glioblastoma stem cells. Oncotarget 2016;7:593–609.
49. Harford-Wright E, Andre-Gregoire G, Jacobs KA, Treps L, Le Gonidec S, Leclair HM, et al. Pharmacological targeting of apelin impairs glioblastoma growth. Brain 2017;140:2939–54.
50. Pitkin SL, Maguire JJ, Kuc RE, Davenport AP. Modulation of the apelin/APJ system in heart failure and atherosclerosis in man. Br J Pharmacol 2010;160:1785–95.
51. De Mota N, Lenkei Z, Llorens-Cortes C. Cloning, pharmacological characterization and brain distribution of the rat apelin receptor. Neuroendocrinology 2000;72:400–7.
52. Zhao H, Tian X, He L, Li Y, Pu W, Liu Q, et al. Apj(+) vessels drive tumor growth and represent a tractable therapeutic target. Cell Rep 2018;25:1241–54.
53. Haynes HR, Camelo-Piragua S, Kurian KM. Prognostic and predictive biomarkers in adult and pediatric gliomas: toward personalized treatment. Front Oncol 2014;4:47.

Published OnlineFirst February 4, 2019; DOI: 10.1158/0008-5472.CAN-18-0881

Cancer Research
The Journal of Cancer Research (1916–1930) | The American Journal of Cancer (1931–1940)

AACR American Association for Cancer Research

Targeting APLN/APLNR Improves Antiangiogenic Efficiency and Blunts Proinvasive Side Effects of VEGFA/VEGFR2 Blockade in Glioblastoma

Giorgia Mastrella, Mengzhuo Hou, Min Li, et al.

Cancer Res 2019;79:2298-2313. Published OnlineFirst February 4, 2019.